


Particles on demand for flows with strong discontinuities

N. G. Kallikounis, B. Dorschner, and I. V. Karlin 

Department of Mechanical and Process Engineering, ETH Zurich, 8092 Zurich, Switzerland



(Received 10 March 2022; accepted 19 May 2022; published 5 July 2022)

Particles-on-demand formulation of kinetic theory [B. Dorschner, F. Bösch and I. V. Karlin, *Phys. Rev. Lett.* **121**, 130602 (2018)] is used to simulate a variety of compressible flows with strong discontinuities in density, pressure, and velocity. Two modifications are applied to the original formulation of the particles-on-demand method. First, a regularization by Grad's projection of particles populations is combined with the reference frame transformations in order to enhance stability and accuracy. Second, a finite-volume scheme is implemented which allows tight control of mass, momentum, and energy conservation. The proposed model is validated with an array of challenging one- and two-dimensional benchmarks of compressible flows, including hypersonic and near-vacuum situations, Richtmyer-Meshkov instability, double Mach reflection, and astrophysical jet. Excellent performance of the modified particles-on-demand method is demonstrated beyond the limitations of other lattice Boltzmann-like approaches to compressible flows.

DOI: [10.1103/PhysRevE.106.015301](https://doi.org/10.1103/PhysRevE.106.015301)

I. INTRODUCTION

The lattice Boltzmann method (LBM) is a recast of fluid dynamics into a fully discrete kinetic system of designed particles with the discrete velocities c_i , $i = 0, \dots, Q - 1$, fitting into a regular space-filling lattice, with the kinetic equation for the populations $f_i(\mathbf{x}, t)$ following a simple algorithm of “stream along links c_i and collide at the nodes \mathbf{x} in discrete time t .” Since its inception [1,2], LBM has evolved into a versatile tool for the simulation of complex flows including transitional flows [3], flows in complex moving geometries [4], thermal and convective flows [5–7], multiphase and multicomponent flows [8–11], and reactive flows [12] and rarefied gas [13], to mention a few recent instances; see Refs. [14–16] for a discussion of LBM and its application areas.

Arguably, LBM is most advantageous for nearly incompressible fluid flow due to exact (lattice) propagation combined with relatively simple discrete velocities, referred to as standard lattices. However, the same features become an obstacle for compressible flows. Several avenues of extending LBM to high-speed flows have been explored. First, a number of proposals proceed with extended sets of discrete velocities while retaining exact lattice propagation [17–19]. LBM with extended sets of discrete velocities demonstrates excellent results [20,21]. However, the gain in both the temperature and Mach number is perceived as moderate when compared to the increased complexity of the higher-order lattices. A second approach uses standard lattices, while LBM is augmented

with corrections terms tailored to eliminate error terms in momentum and energy equations [22–25]. While trans- and supersonic flows can be captured efficiently with this approach, it, too, remained limited to moderate Mach number and discontinuities.

Another line of research abandons the restriction of lattice-fitting discrete velocities and proposes a less rigid off-lattice propagation. While originally conceived for standard velocity sets in order to gain geometrical flexibility [26–28], off-lattice propagation schemes received some traction more recently in the context of compressible flows. Interesting realizations for compressible flows at moderate Mach numbers using a semi-Lagrangian advection have recently been reported in Refs. [29–31]. Another class of numerical schemes are finite-volume methods, such as the discrete unified gas kinetic scheme (DUGKS) [32,33]. Finite-difference propagation was used in the discrete Boltzmann model targeting compressible flows with applications to combustion and detonation [34–38].

Regardless of the propagation scheme (on- or off-lattice), a common feature of the above models is the use of fixed discrete velocities which amounts to choosing the reference frame “at rest.” While the latter is viable and even advantageous (due to lattice propagation) for nearly incompressible, slow flows, it impedes the use of kinetic-theory-based solvers for high Mach number situations. Examples of a better reference frame are readily available. For instance, in Ref. [39], the formulation of LBM in a comoving Galilean reference frame demonstrated excellent performance for predominantly unidirectional compressible flows. Subsequently, the particles-on-demand (PonD) method [40] addressed the problem of finding the optimal reference frame. In PonD, the discrete particle velocities are constructed relative to the local reference frame, which is defined by the local flow velocity and temperature and which varies in space and time. This necessitates an off-lattice propagation scheme, together with a

*Corresponding author: ikarlin@ethz.ch

Published by the American Physical Society under the terms of the Creative Commons Attribution 4.0 International license. Further distribution of this work must maintain attribution to the author(s) and the published article's title, journal citation, and DOI.

reference frame transformation to resolve the implicitness of the PonD scheme.

In this work, we aim at a further development of PonD in order to enable simulations at extreme cases of compressible flows. First, the reference frame transformation is supplemented with a regularization procedure based on Grad's projection. In the framework of PonD, regularization was recently suggested in Ref. [41], with the purpose of reducing the computational cost. Here we show that a carefully tailored moment system, serving as a basis for the transformation, enables PonD to simulate flows with strong discontinuities. Second, in addition to the semi-Lagrangian realization, we propose a finite-volume version of the PonD, based on the appropriate extension of the DUGKS method. This enables a tight control of the conservation laws which becomes especially important for flows with near-vacuum components. It is noted that high Mach number flows, with near-vacuum regions and strong discontinuities, remain active area of research in classical computational fluid dynamics (CFD), with recent development of higher-order schemes such as targeted essentially nonoscillatory, besides more established shock-capturing methods [42–44]. The proposed model is able to capture complicated flows robustly and accurately, without the need of positivity preserving schemes and sophisticated limiters [43].

The paper is organized as follows. In Sec. II, the two-population kinetic model is introduced and the reference frame transformation is explained. Subsequently, in Sec. III the semi-Lagrangian and the finite-volume discretization schemes are presented. In Sec. IV, the model is validated against extreme one-dimensional Riemann problems and various two-dimensional benchmarks. Finally, concluding remarks are provided in Sec. V.

II. MODEL DESCRIPTION

A. Discrete velocities

Without a loss of generality, we consider discrete speeds in two dimensions formed by tensor products of roots of Hermite polynomials $c_{i\alpha}$,

$$\mathbf{c}_i = (c_{ix}, c_{iy}). \quad (1)$$

The model is characterized by the lattice temperature T_L and the weights W_i associated with the vectors (1),

$$W_i = w_{ix}w_{iy}, \quad (2)$$

where $w_{i\alpha}$ are weights of the Gauss-Hermite quadrature. In this work we use the D2Q16 velocity set, where $D = 2$ stands for two dimensions and $Q = 16$ is the number of the discrete velocities. The discrete velocities and the associated weights are shown in Table I. With the discrete speeds (1), the particles' velocities \mathbf{v}_i are defined relative to a reference frame, specified by the frame velocity \mathbf{u}_{ref} and the reference temperature T_{ref} ,

$$\mathbf{v}_i = \sqrt{\frac{T_{\text{ref}}}{T_L}} \mathbf{c}_i + \mathbf{u}_{\text{ref}}. \quad (3)$$

The optimal reference frame is the comoving reference frame, which is specified by the *local* temperature $T_{\text{ref}} = T(\mathbf{x}, t)$ and

TABLE I. Lattice temperature T_L , roots of Hermite polynomials $c_{i\alpha}$, and weights $w_{i\alpha}$ of the $D = 1$ Gauss-Hermite quadrature and nomenclature

| Model | T_L | $c_{i\alpha}$ | $w_{i\alpha}$ | $D = 2$ |
|-------|-------|--------------------------|---------------------|---------|
| D1Q3 | 1 | 0, | 2/3 | D2Q9 |
| | | $\pm\sqrt{3}$ | 1/6 | |
| D1Q4 | 1 | $\pm\sqrt{3 - \sqrt{6}}$ | $(3 + \sqrt{6})/12$ | D2Q16 |
| | | $\pm\sqrt{3 + \sqrt{6}}$ | $(3 - \sqrt{6})/12$ | |

the *local* flow velocity $\mathbf{u}_{\text{ref}} = \mathbf{u}(\mathbf{x}, t)$.

B. Kinetic equations

In this paper, we restrict our consideration to a single relaxation time, two-population kinetic model for ideal gas with variable adiabatic exponent [20],

$$\partial_t f_i + \mathbf{v}_i \cdot \nabla f_i = \Omega_{f,i} = \frac{1}{\tau} (f_i^{\text{eq}} - f_i), \quad (4)$$

$$\partial_t g_i + \mathbf{v}_i \cdot \nabla g_i = \Omega_{g,i} = \frac{1}{\tau} (g_i^{\text{eq}} - g_i), \quad (5)$$

where f_i^{eq} and g_i^{eq} are local equilibrium populations and τ is the relaxation time. Local conservation laws for the density ρ , momentum $\rho\mathbf{u}$, and the total energy ρE are

$$\rho = \sum_{i=0}^{Q-1} f_i = \sum_{i=0}^{Q-1} f_i^{\text{eq}}, \quad (6)$$

$$\rho\mathbf{u} = \sum_{i=0}^{Q-1} \mathbf{v}_i f_i = \sum_{i=0}^{Q-1} \mathbf{v}_i f_i^{\text{eq}}, \quad (7)$$

$$\rho E = \sum_{i=0}^{Q-1} \frac{v_i^2}{2} f_i + \sum_{i=0}^{Q-1} g_i = \sum_{i=0}^{Q-1} \frac{v_i^2}{2} f_i^{\text{eq}} + \sum_{i=0}^{Q-1} g_i^{\text{eq}}, \quad (8)$$

where the total energy of ideal gas is

$$\rho E = C_v \rho T + \frac{\rho u^2}{2}, \quad (9)$$

with C_v the specific heat at constant volume. In the comoving reference frame, the equilibrium populations depend only on the density and temperature,

$$f_i^{\text{eq}} = \rho W_i, \quad (10)$$

$$g_i^{\text{eq}} = \left(C_v - \frac{D}{2} \right) T \rho W_i. \quad (11)$$

The single relaxation time Bhatnagar-Gross-Krook (BGK) model (4) and (5) results in a Prandtl number equal to 1. This restriction is adopted in the present study for the sake of presentation since the benchmark cases considered below refer to nondissipative compressible flow. Extension of the present model to a variable Prandtl number can be found in Refs. [20,45].

C. Regularized reference frame transformation

Let us consider a reference frame λ defined by a reference temperature T and frame velocity \mathbf{u} ,

$$\lambda = \{\mathbf{u}, T\}. \quad (12)$$

Discrete velocities relative to the reference frame λ (12) are defined as

$$\mathbf{v}_i^\lambda = \sqrt{\frac{T}{T_L}} \mathbf{c}_i + \mathbf{u}. \quad (13)$$

In order to keep the notation simple, we shall consider f populations (g populations are considered in the same fashion). A key element of PonD is the transformation of populations f_i^λ , defined with respect to a λ reference (12), to a different reference frame λ' ,

$$\lambda' = \{\mathbf{u}', T'\}, \quad (14)$$

with the discrete velocities $\mathbf{v}_i^{\lambda'}$,

$$\mathbf{v}_i^{\lambda'} = \sqrt{\frac{T'}{T_L}} \mathbf{c}_i + \mathbf{u}'. \quad (15)$$

Below, the transformation proposed in Ref. [40] is supplemented by a regularization procedure [41,46]. Specifically, the transformed populations $f_i^{\lambda'}$ are sought as a third-order Grad's projection,

$$f_i^{\lambda'} = W_i \left[a_0 + \frac{\mathbf{a}_1 \cdot \mathbf{c}_i}{T_L} + \frac{\mathbf{a}_2 \cdot (\mathbf{c}_i \otimes \mathbf{c}_i - T_L \mathbf{I})}{2T_L^2} + \frac{\mathbf{a}_3 \cdot (\mathbf{c}_i \otimes \mathbf{c}_i \otimes \mathbf{c}_i - T_L \overline{\mathbf{c}_i \otimes \mathbf{c}_i \otimes \mathbf{c}_i})}{6T_L^3} \right], \quad (16)$$

where overline denotes symmetrization, coefficients \mathbf{a}_k are tensors of rank $k = 0$ to $k = 3$, while the dot stands for the full contraction. Let us denote \mathbf{M}_k^λ a moment tensor of order k ,

$$\mathbf{M}_k^\lambda = \sum_{i=0}^{Q-1} f_i^\lambda \underbrace{\mathbf{v}_i^\lambda \otimes \mathbf{v}_i^\lambda \cdots \otimes \mathbf{v}_i^\lambda}_k. \quad (17)$$

Then the regularized transformed populations are defined by the condition of invariance of the moments of orders $k = 0, 1, 2, 3$ with respect to the reference frame:

$$\mathbf{M}_k^{\lambda'} = \mathbf{M}_k^\lambda, \quad k = 0, 1, 2, 3. \quad (18)$$

On substitution,

$$\mathbf{M}_k^{\lambda'} = \sum_{i=0}^{Q-1} f_i^{\lambda'} \underbrace{\mathbf{v}_i^{\lambda'} \otimes \mathbf{v}_i^{\lambda'} \cdots \otimes \mathbf{v}_i^{\lambda'}}_k, \quad k = 0, 1, 2, 3,$$

and using (16) and (15), the linear system (18) is solved to find Grad's coefficients \mathbf{a}_k , $k = 0, 1, 2, 3$ in terms of the new frame velocity \mathbf{u}' , reference temperature T' , and the moments in the old reference frame \mathbf{M}_k^λ ,

$$a_0 = M_0^\lambda, \quad (19)$$

$$\mathbf{a}_1 = \left(\frac{T'}{T_L} \right)^{-1/2} (\mathbf{M}_1^\lambda - M_0^\lambda \mathbf{u}'), \quad (20)$$

$$\mathbf{a}_2 = \left(\frac{T'}{T_L} \right)^{-1} \left[\mathbf{M}_2^\lambda - M_0^\lambda T' \mathbf{I} - \left(\frac{T'}{T_L} \right)^{1/2} \overline{\mathbf{u}' \otimes \mathbf{a}_1} - M_0^\lambda \mathbf{u}' \otimes \mathbf{u}' \right], \quad (21)$$

$$\begin{aligned} \mathbf{a}_3 = & \left(\frac{T'}{T_L} \right)^{-3/2} \left[\mathbf{M}_3^\lambda - \left(\frac{T'}{T_L} \right) \overline{\mathbf{u}' \otimes (M_0 T_L \mathbf{I} + \mathbf{a}_2)} \right. \\ & - T' \left(\frac{T'}{T_L} \right)^{1/2} \overline{\mathbf{a}_1 \otimes \mathbf{I}} - \left(\frac{T'}{T_L} \right)^{1/2} \overline{\mathbf{a}_1 \otimes \mathbf{u}' \otimes \mathbf{u}'} \\ & \left. - M_0^\lambda \mathbf{u}' \otimes \mathbf{u}' \otimes \mathbf{u}' \right]. \end{aligned} \quad (22)$$

Thus, the regularized transformation of the f populations from a reference frame λ to a reference frame λ' is uniquely defined by the third-order Grad's projection with the coefficients (19), (20), (21), and (22). For the regularized transformation of the g populations, it is sufficient to use a second-order Grad's projection of the form (16) where the third-order term is dropped while the coefficients a_0 , \mathbf{a}_1 , and \mathbf{a}_2 are defined by (19), (20), and (21), respectively, with the corresponding moments \mathbf{M}_k^λ , $k = 0, 1, 2$, of the populations g_i^λ . A discussion is in order.

(i) A rationale for using Grad's projection for regularized transformation is to essentially impose a moment hierarchy in the new reference frame: The low-order moments retained in Grad's projection [\mathbf{M}_k , $k = 0, 1, 2, 3$ in the case of Eq. (16)] are independent and can be identified as "slow" moments. The remaining higher-order moments are considered as "fast" moments, enslaved by the slow ones and given by Grad's closure [47].

(ii) Grad's projection is not a unique regularization strategy. For instance, another possibility is to set the higher-order moments to equilibrium following the construction proposed in Ref. [45]: Let us denote $M_q = \{\mathbf{M}_0, \mathbf{M}_1, \mathbf{M}_2, \mathbf{M}_3\}$ the subset of slow moments, where q is the dimension of the subspace, $q = 10$ for $D = 2$ and $q = 20$ for $D = 3$, while M_{Q-q} stands for the fast moments. Moment vector of the f populations M_Q can be considered as an element of a direct sum,

$$M_Q = M_q \oplus M_{Q-q}. \quad (23)$$

In the new reference frame λ' , consider a moment vector $M_Q^{\lambda \rightarrow \lambda'}$ using the λ frame to evaluate the slow moments, $M_q^{\lambda'} = M_q^\lambda$, as before, while equilibrating the fast moments in the λ' reference:

$$M_Q^{\lambda \rightarrow \lambda'} = M_q^\lambda \oplus (M_{Q-q}^{\lambda'})^{\text{eq}}. \quad (24)$$

The regularized transformed populations are obtained by moment inversion,

$$f^{\lambda'} = \mathcal{M}_{\lambda'}^{-1} M_Q^{\lambda \rightarrow \lambda'}, \quad (25)$$

where $\mathcal{M}_{\lambda'}$ is the $Q \times Q$ matrix of the populations-to-moments transform in the λ' reference frame. The difference between the two regularization methods is that, with Grad's projection, the fast moments are slaved to the nonequilibrium

slow moments, $M_{Q-q}^{\text{Grad}} = M_{Q-q}(M_q)$, while in the equilibration case they are $M_{Q-q}^{\text{eq}} = M_{Q-q}^{\text{eq}}(M_0, \mathbf{M}_1)$. While both approaches are on equal footing, Grad's projection appears to be more economic as it does not need a matrix inversion (25) and shall be used below in this paper.

(iii) In two dimensions, the $D2Q16$ lattice is the minimal product-form lattice based on Hermite roots that has a linearly independent third-order moment tensor \mathbf{M}_3 and therefore enables the third-order Grad's projection (16). While some previous realizations of PonD method for compressible flows used the standard $D2Q9$ lattice [40,48,49], inclusion of \mathbf{M}_3 into the list of slow moments appears to be necessary in order to simulate hypersonic flows with very strong discontinuities and near-vacuum components such as those presented in Sec. IV B.

III. SEMI-LAGRANGIAN AND FINITE VOLUME REALIZATIONS

In this section, we present two methods for the numerical discretization of the proposed PonD model. First, we review the semi-Lagrangian scheme, as formulated in Refs. [40,48,49]. A finite-volume method, based on the DUGKS numerical scheme [32], is subsequently presented.

A. Semi-Lagrangian realization

The semi-Lagrangian realization follows the spirit of LBM, where the governing continuous equations (4) and (5) are integrated along the characteristics and a variable transformation is used to eliminate the implicitness of the scheme [5,50],

$$\tilde{f}_i = f_i - \frac{\delta t}{2\tau} (f_i^{\text{eq}} - f_i), \quad (26)$$

$$\tilde{g}_i = g_i - \frac{\delta t}{2\tau} (g_i^{\text{eq}} - g_i). \quad (27)$$

The final equations, which describe the propagation and collision steps, can be expressed only through the \tilde{f} and \tilde{g} populations. For simplicity, we lift in this section the tilde notation. The spatiotemporal flexibility of the reference frame leads to an off-lattice propagation, which requires the reconstruction of the populations at any point \mathbf{x} and time t . In this work, we use the following formula [40]:

$$f_i(\mathbf{x}, t) = \sum_{s=1}^m \Lambda(\mathbf{x} - \mathbf{x}_s) f_i^\lambda(\mathbf{x}_s, t), \quad (28)$$

$$g_i(\mathbf{x}, t) = \sum_{s=1}^m \Lambda(\mathbf{x} - \mathbf{x}_s) g_i^\lambda(\mathbf{x}_s, t), \quad (29)$$

where \mathbf{x}_s are the collocation points and Λ is the interpolation kernel and it is assumed that regularized populations at the collocation points, $f_i^\lambda(\mathbf{x}_s, t)$ and $g_i^\lambda(\mathbf{x}_s, t)$, are transformed into the same reference frame λ , as explained in Sec. II C. Below, we use a four-point stencil ($m = 4$) with a B-spline interpolation kernel in a combination with limiters, as detailed in Ref. [51].

We consider the propagation step at a monitoring point \mathbf{x} and time t . Semi-Lagrangian advection is performed at the departure points of characteristic lines $\mathbf{x} - \mathbf{v}_i^{\lambda_0} \delta t$,

$$f_i^{\lambda_0} = f_i(\mathbf{x} - \mathbf{v}_i^{\lambda_0} \delta t, t - \delta t), \quad (30)$$

$$g_i^{\lambda_0} = g_i(\mathbf{x} - \mathbf{v}_i^{\lambda_0} \delta t, t - \delta t). \quad (31)$$

The reference frame $\lambda_0 = \{\mathbf{u}_0, T_0\}$ is initialized using the local flow velocity and the local temperature, which are available from the previous time step, $\mathbf{u}_0 = \mathbf{u}(\mathbf{x}, t - \delta t)$, $T_0 = T(\mathbf{x}, t - \delta t)$. Equations (30) and (31) constitute the predictor propagation step. The density, momentum, and temperature are consequently computed by

$$\rho_1 = \sum_{i=0}^{Q-1} f_i^{\lambda_0}, \quad (32)$$

$$\rho_1 \mathbf{u}_1 = \sum_{i=0}^{Q-1} \mathbf{v}_i^{\lambda_0} f_i^{\lambda_0}, \quad (33)$$

$$\rho_1 E_1 = \sum_{i=0}^{Q-1} \frac{(\mathbf{v}_i^{\lambda_0})^2}{2} f_i^{\lambda_0} + \sum_{i=0}^{Q-1} g_i^{\lambda_0}. \quad (34)$$

The computed velocity (33) and temperature (34) define the corrector reference frame $\lambda_1 = \{\mathbf{u}_1, T_1\}$ at the monitoring point and the propagation step (30) and (31) is repeated with the updated reference frame. The predictor-corrector process is iterated until convergence with the limit values,

$$\rho(\mathbf{x}, t), \mathbf{u}(\mathbf{x}, t), T(\mathbf{x}, t), f_i^{\lambda(\mathbf{x}, t)} = \lim_{n \rightarrow \infty} \rho_n, \mathbf{u}_n, T_n, f_i^{\lambda_n},$$

defining the density, velocity, temperature, and the pre-collision populations at the monitoring point \mathbf{x} at time t . The predictor-corrector iteration loop ensures that the propagation and the collision steps are performed at the comoving reference frame, in which the local equilibrium populations (10) and (11) are exact.

The collision step follows the BGK collision model,

$$f_i(\mathbf{x}, t) = f_i^{\lambda(\mathbf{x}, t)} + 2\beta [\rho(\mathbf{x}, t) W_i - f_i^{\lambda(\mathbf{x}, t)}], \quad (35)$$

$$g_i(\mathbf{x}, t) = g_i^{\lambda(\mathbf{x}, t)} + 2\beta \left[\rho \left(C_v - \frac{D}{2} \right) T(\mathbf{x}, t) W_i - g_i^{\lambda(\mathbf{x}, t)} \right], \quad (36)$$

where the relaxation parameter β is related to the kinematic viscosity by $\nu = T(\frac{1}{2\beta} - \frac{1}{2})\delta t$. The thermal conductivity is $\kappa = C_p(\frac{1}{2\beta} - \frac{1}{2})\rho T \delta t$, which yields Prandtl equal to 1.

B. Finite-volume realization

The semi-Lagrangian propagation, coupled with a local collision step, is a simple and efficient numerical scheme for the realization of PonD. It should be noted, however, that this

method is not strictly conservative. While there exist strategies to partially alleviate this problem [51–53], we propose a finite-volume discretization scheme which naturally restores the conservation. Specifically, we reformulate the DUGKS algorithm [32,33,54] in a comoving reference frame.

1. Updating rule

The evolution of the populations is governed by the following equations in the DUGKS framework [32]:

$$\begin{aligned}\tilde{f}_i(\mathbf{x}_j, t_{n+1}) &= \left(\frac{2\tau - \delta t}{2\tau + \delta t} \right) \tilde{f}_i(\mathbf{x}_j, t_n) \\ &+ \left(\frac{2\delta t}{2\tau + \delta t} \right) f_i^{\text{eq}}(\mathbf{x}_j, t_n) - \frac{\delta t}{V_j} F_{f,i}(\mathbf{x}_j, t_{n+1/2}),\end{aligned}\quad (37)$$

$$\begin{aligned}\tilde{g}_i(\mathbf{x}_j, t_{n+1}) &= \left(\frac{2\tau - \delta t}{2\tau + \delta t} \right) \tilde{g}_i(\mathbf{x}_j, t_n) \\ &+ \left(\frac{2\delta t}{2\tau + \delta t} \right) g_i^{\text{eq}}(\mathbf{x}_j, t_n) - \frac{\delta t}{V_j} F_{g,i}(\mathbf{x}_j, t_{n+1/2}).\end{aligned}\quad (38)$$

The update equations are derived from the integration of the continuous equations (4) and (5) in a control volume centered at \mathbf{x}_j , with volume V_j , from time t_n to $t_{n+1} = t_n + \delta t$, using the midpoint rule for the convection term and the trapezoidal rule for the collision term [32]. To remove the implicitness,

the DUGKS scheme adopts the variable transformation from the standard LBM practice [5,50],

$$\tilde{\phi}_i = \phi_i - \frac{\delta t}{2} \Omega_{\phi,i} = \phi_i - \frac{\delta t}{2\tau} (\phi_i^{\text{eq}} - \phi_i), \quad (39)$$

where ϕ stands for the f and g populations and $\Omega_{\phi,i}$ are the collision BGK kernels defined in Eqs. (4) and (5). The fluxes of the populations $F_{\phi,i}(\mathbf{x}_j, t_{n+1/2})$ across the surface of the control volume are defined as

$$F_{\phi,i}(\mathbf{x}_j, t_{n+1/2}) = \int_{\partial V_j} (\mathbf{v}_i \cdot \mathbf{n}) \phi_i(\mathbf{x}, t_{n+1/2}) dS, \quad (40)$$

where \mathbf{n} is the outward unit vector normal to the surface. Finally, we remark that within the finite-volume context, the populations and the collision terms are cell-averaged quantities,

$$\phi_i(\mathbf{x}_j, t_n) = \frac{1}{V_j} \int_{V_j} \phi_i(\mathbf{x}, t_n) d\mathbf{x}. \quad (41)$$

2. Evolution in the comoving reference frame

In this section, we present the implementation of DUGKS with an adaptive reference frame formulation. We consider a cell with center \mathbf{x}_j , at time t_n . The populations $f_i^\lambda(\mathbf{x}_j, t_n)$, $g_i^\lambda(\mathbf{x}_j, t_n)$ are known from the previous time step (or initial conditions) and they are expressed in the local reference frame $\lambda = \{\mathbf{u}(\mathbf{x}_j, t_n), T(\mathbf{x}_j, t_n)\}$. With the exact equilibria (10) and (11), the update equations become

$$\tilde{f}_i^\lambda(\mathbf{x}_j, t_{n+1}) = \left(\frac{2\tau - \delta t}{2\tau + \delta t} \right) \tilde{f}_i^\lambda(\mathbf{x}_j, t_n) + \left(\frac{2\delta t}{2\tau + \delta t} \right) \rho(\mathbf{x}_j, t_n) W_i - \frac{\delta t}{V_j} F_{f,i}^\lambda(\mathbf{x}_j, t_{n+1/2}), \quad (42)$$

$$\tilde{g}_i^\lambda(\mathbf{x}_j, t_{n+1}) = \left(\frac{2\tau - \delta t}{2\tau + \delta t} \right) \tilde{g}_i^\lambda(\mathbf{x}_j, t_n) + \left(\frac{2\delta t}{2\tau + \delta t} \right) \left(C_v - \frac{D}{2} \right) \rho(\mathbf{x}_j, t_n) T(\mathbf{x}_j, t_n) W_i - \frac{\delta t}{V_j} F_{g,i}^\lambda(\mathbf{x}_j, t_{n+1/2}). \quad (43)$$

The fluxes (40) featured in the update equations (42) and (43) are evaluated in the next section.

3. Flux evaluation in the comoving reference frame

The key element of the update equations (42) and (43) is the evaluation of the flux term, $F_{\phi,i}(\mathbf{x}_j, t_{n+1/2})$, which contains the unknown populations $\phi_i(\mathbf{x}_b, t_{n+1/2})$ at the cell interface \mathbf{x}_b and time $t_{n+1/2}$. Integrating Eqs. (4) and (5) along the characteristics for half-time step shows that the requested populations are connected with the known populations at time t_n through the following equation [32]:

$$\bar{\phi}_i(\mathbf{x}_b, t_{n+1/2}) = \bar{\phi}_i^+(\mathbf{x}_b - \mathbf{v}_i \delta t/2, t_n), \quad (44)$$

where

$$\bar{\phi}_i = \phi_i - \frac{\delta t/2}{2} \Omega_{\phi,i}, \quad (45)$$

$$\bar{\phi}_i^+ = \phi_i + \frac{\delta t/2}{2} \Omega_{\phi,i}. \quad (46)$$

Equation (44) is essentially a half-time step semi-Lagrangian advection step, as in LBM, with the final point located at the interface \mathbf{x}_b , at $t_{n+1/2}$. Following the spirit of PonD, we realize this step in the comoving reference frame, with the following iterating procedure.

The reference frame $\lambda_0 = \{\mathbf{u}_0, T_0\}$ (predictor reference frame) at the cell interface \mathbf{x}_b is initialized with the fluid velocity and temperature from the previous step, $\mathbf{u}_0 = \mathbf{u}(\mathbf{x}_b, t_{n-1/2})$, $T_0 = T(\mathbf{x}_b, t_{n-1/2})$. The populations $\bar{\phi}_i^{+, \lambda_0}$ and the spatial gradients $\sigma_i^{\lambda_0} = \nabla \bar{\phi}_i^{+, \lambda_0}$ are subsequently evaluated in the neighboring cells of the interface, at time t_n . In this work, Van Leer and minmod slope limiters were used for the computation of the spatial derivatives [55,56]. We also note that the regularized reference frame transformation is applied, to express the required populations from their original reference frame to the target reference frame λ_0 . The populations are reconstructed at the departure point $\mathbf{x}' = \mathbf{x}_b - \mathbf{v}_i^{\lambda_0} \delta t/2$, with the MUSCL scheme [57],

$$\bar{\phi}_i^{+, \lambda_0}(\mathbf{x}', t_n) = \bar{\phi}_i^{+, \lambda_0}(\mathbf{x}_j, t_n) + (\mathbf{x}' - \mathbf{x}_j) \cdot \sigma_i^{\lambda_0}(\mathbf{x}_j, t_n). \quad (47)$$

According to Eq. (44), we obtain the $\bar{\phi}_i^{\lambda_0}$ populations at the interface \mathbf{x}_b and time $t_{n+1/2}$ by

$$\bar{\phi}_i^{\lambda_0}(\mathbf{x}_b, t_{n+1/2}) = \bar{\phi}_i^{+, \lambda_0}(\mathbf{x}', t_n). \quad (48)$$

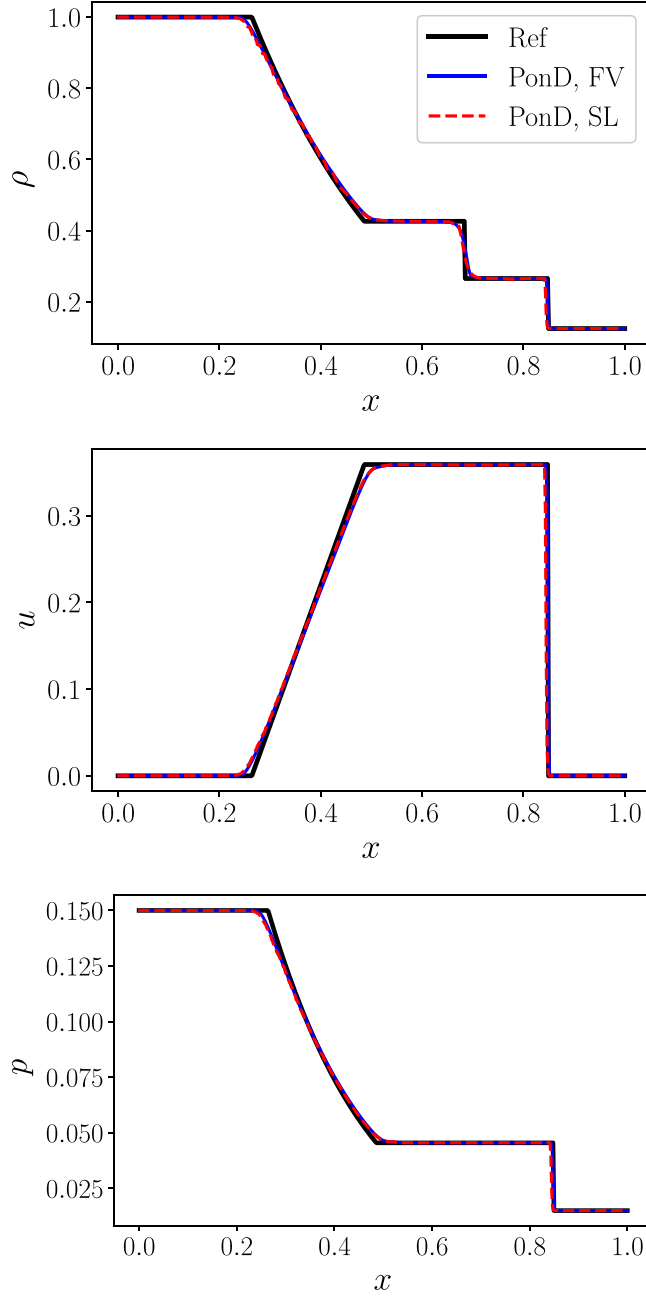


FIG. 1. Density (top), velocity (middle), and pressure (bottom) profiles for Sod's shock tube, at $t = 0.2$. Dashed line: Semi-Lagrangian (SL) scheme. Solid line: Finite-volume (FV) scheme. Thick solid line: Reference from an exact Riemann solver.

The density, momentum, and temperature are finally computed by

$$\rho_1 = \sum_{i=0}^{Q-1} \tilde{f}_i^{\lambda_0}(\mathbf{x}_b, t_{n+1/2}), \quad (49)$$

$$\rho_1 \mathbf{u}_1 = \sum_{i=0}^{Q-1} \mathbf{v}_i^{\lambda_0} \tilde{f}_i^{\lambda_0}(\mathbf{x}_b, t_{n+1/2}), \quad (50)$$

$$\rho_1 E_1 = \sum_{i=0}^{Q-1} \frac{(\mathbf{v}_i^{\lambda_0})^2}{2} \tilde{f}_i^{\lambda_0}(\mathbf{x}_b, t_{n+1/2}) + \sum_{i=0}^{Q-1} \tilde{g}_i^{\lambda_0}(\mathbf{x}_b, t_{n+1/2}). \quad (51)$$

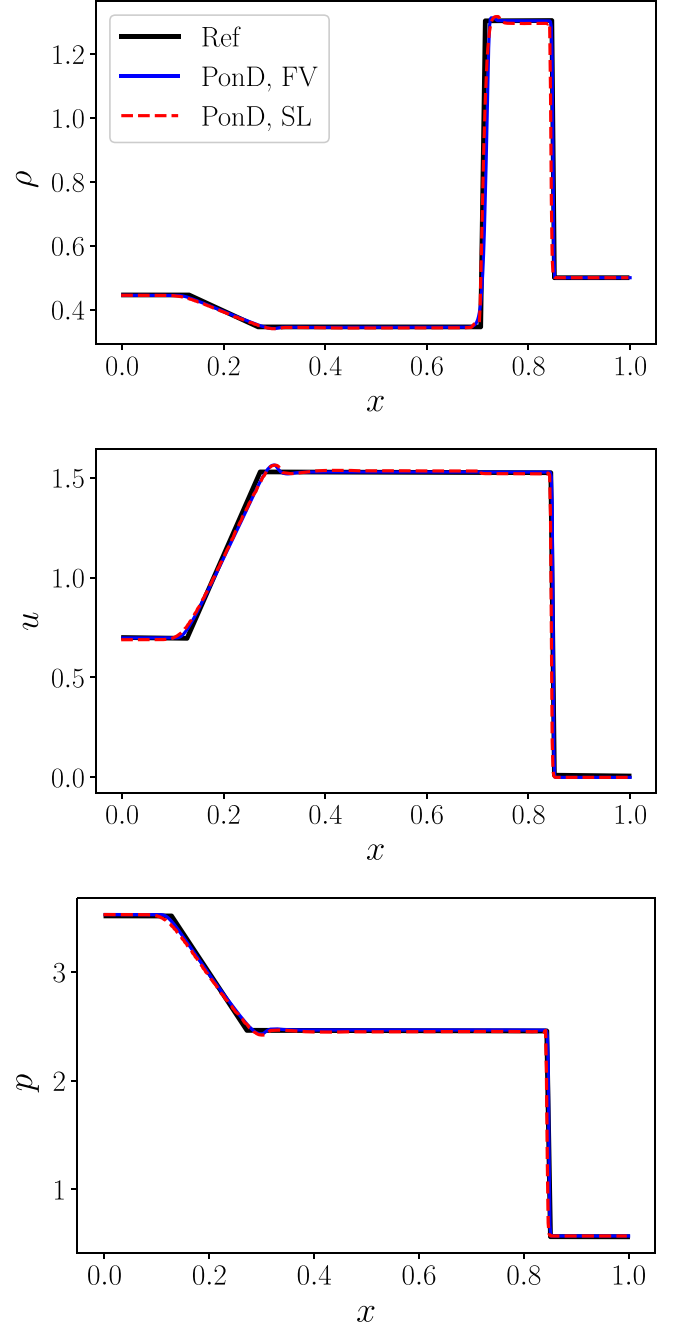


FIG. 2. Density (top), velocity (middle), and pressure (bottom) profiles for Lax problem at $t = 0.14$. Dashed line: Semi-Lagrangian (SL) scheme. Solid line: Finite-volume (FV) scheme. Thick solid line: Reference from an exact Riemann solver.

The computed moments define the corrector reference frame $\lambda_1 = \{\mathbf{u}_1, T_1\}$. We repeat the above half-time step semi-Lagrangian advection step with the updated λ_1 and the predictor-corrector loop is continued on reference frame convergence $\lambda_b = \lim_{k \rightarrow \infty} \lambda_k(\mathbf{x}_b, t_{n+1/2})$. With this procedure we enforce the execution of the advection at the optimal comoving reference frame. With the completion of the advection, Eq. (45) is used to obtain the populations $\phi_i^{\lambda_b}(\mathbf{x}_b, t_{n+1/2})$, where the equilibria that are needed are the exact comoving equilibria (10) and (11). The flux of the populations across

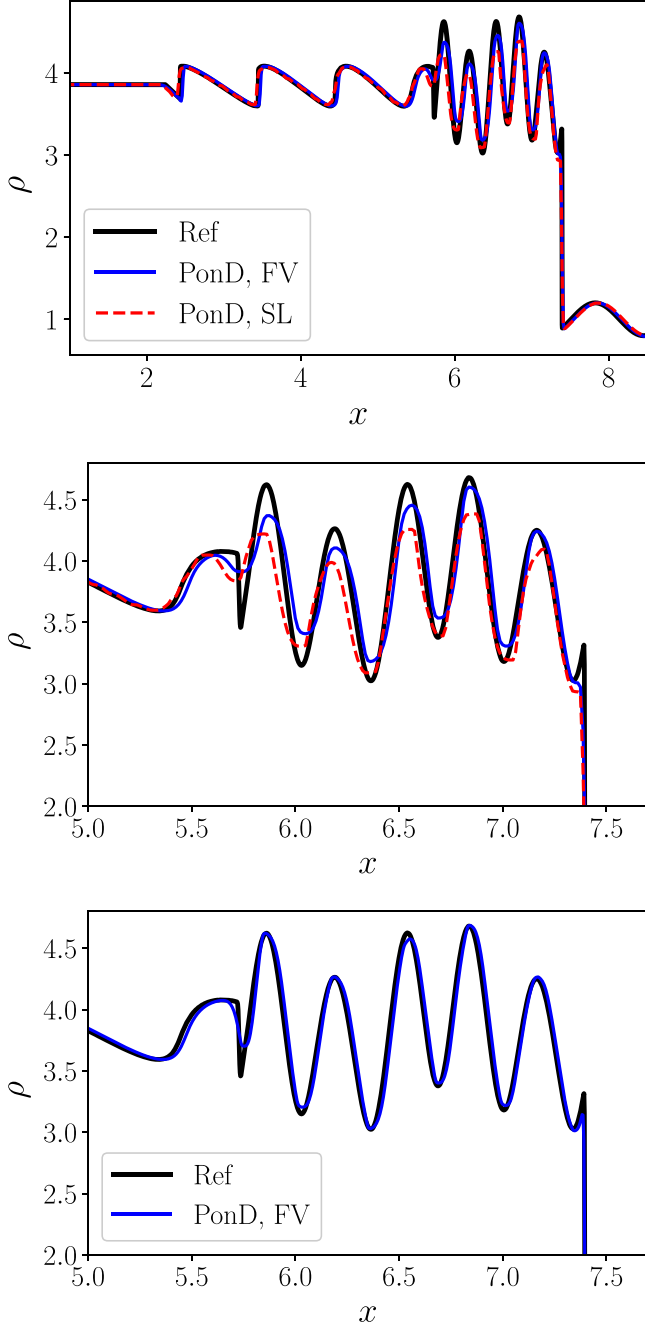


FIG. 3. Density profile for the Shu-Osher problem at $t = 1.8$. Dashed line: Semi-Lagrangian (SL) scheme. Solid line: Finite-volume (FV) scheme. Thick solid line: Reference solution [61], obtained with characteristic-based fifth order WENO, RK4 temporal integration and resolution of 5000 points. Middle: A zoom into the high-frequency wave region. Bottom: FV scheme with high resolution $L = 2400$.

the interface of the cell \mathbf{x}_j , in the local reference frame λ , can then be computed as

$$F_{\phi,i}^\lambda(\mathbf{x}_j, t_{n+1/2}) = \sum_c (\mathbf{v}_i^\lambda \cdot \mathbf{n}_c) \phi_i^\lambda(\mathbf{x}_{b,c}, t_{n+1/2}), \quad (52)$$

where $\mathbf{x}_{b,c}$ designates the center of the c th face of the cell and \mathbf{n}_c is the outwards normal vector.

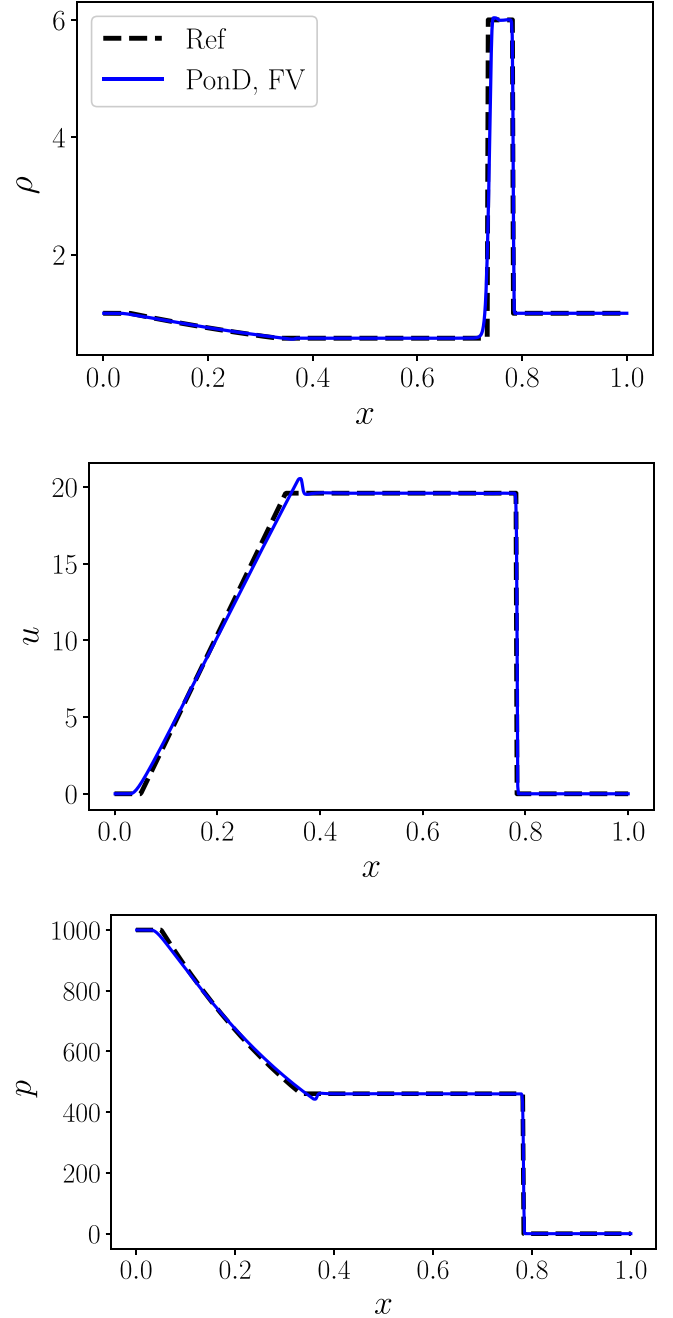


FIG. 4. Density (top), velocity (middle), and pressure (bottom) profiles for the strong shock tube problem at $t = 0.012$. Solid line: Finite-volume (FV) scheme. Dashed line: Reference from an exact Riemann solver.

4. Summary of the algorithm

Based on the previous steps, we summarize the evolution procedure from time t_n to t_{n+1} :

- (1) Initialization of the populations

Loop over cell centers \mathbf{x}_j : The populations $\tilde{\phi}_i(\mathbf{x}_j, t_n)$ are expressed according to local reference frame, $\lambda = \{\mathbf{u}(\mathbf{x}_j, t_n), T(\mathbf{x}_j, t_n)\}$.

- (2) Calculation of the fluxes

Loop over cell centers \mathbf{x}_j : Calculation of the $\bar{\phi}_i^+(\mathbf{x}_j, t_n)$ populations, according to Eq. (46).

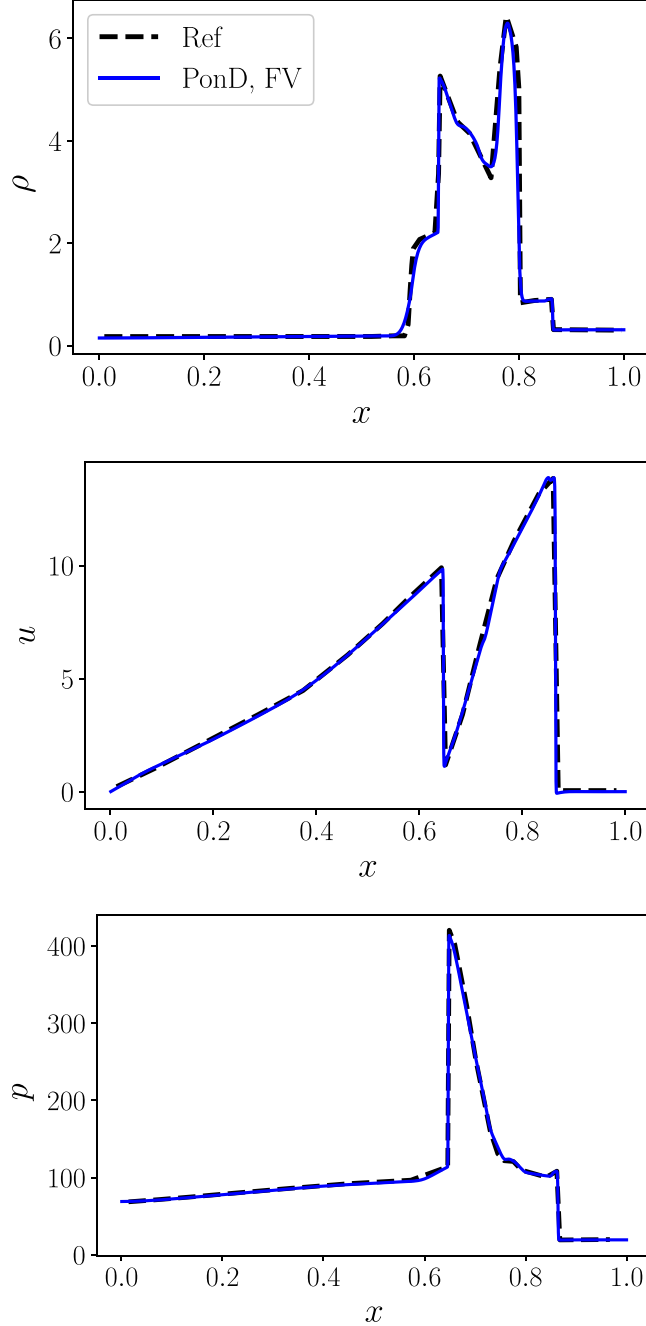


FIG. 5. Density (top), velocity (middle), and pressure (bottom) profiles for the two blast wave problem, at $t = 0.038$. Solid line: Finite-volume (FV) scheme. Dashed line: Reference solution [42].

Loop over cell faces x_b : Calculation of the populations $\phi_i(x_b, t_{n+1/2})$ at the comoving reference frame, according to the iteration procedure in Sec. III B 3.

(3) Population update

Loop over cell centers x_j : Computation of the fluxes to the local reference frame of the cell Eq. (52) and update the populations through Eqs. (42) and (43).

It is interesting to underline the differences between the proposed formulation in the optimal reference frame and the original DUGKS scheme [32]. First we note that in the proposed scheme, the reference frame is adaptive in space and

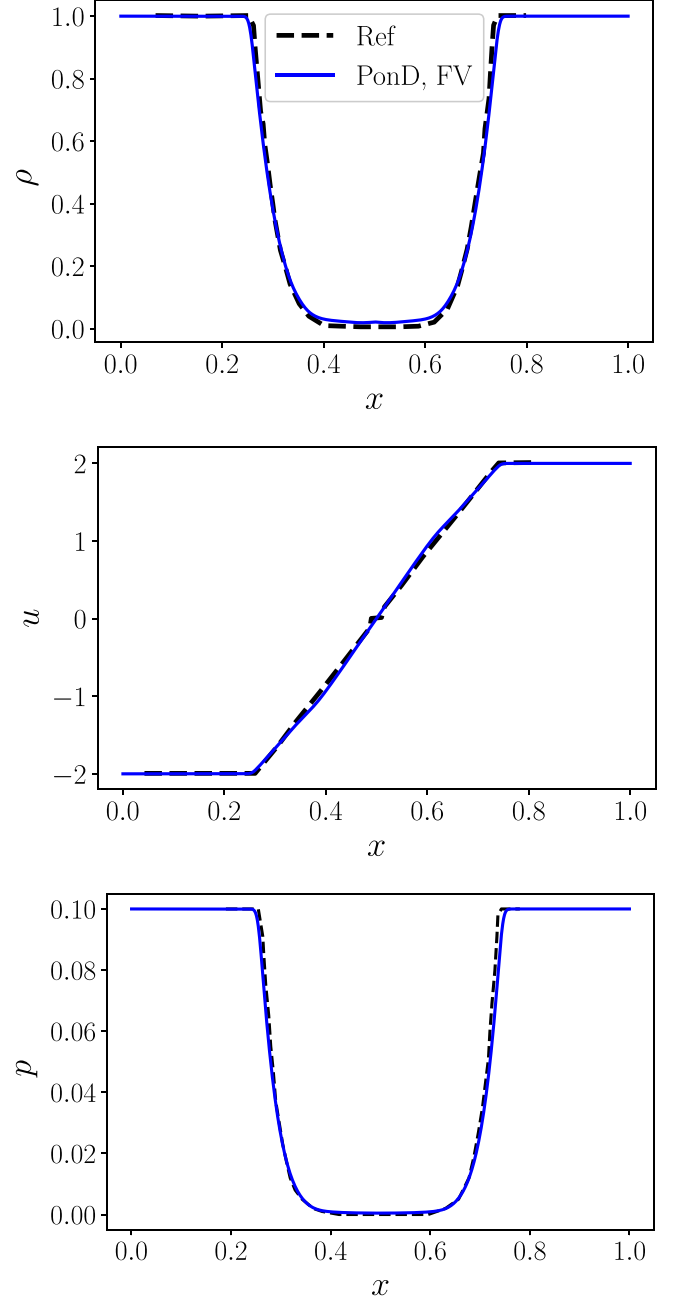


FIG. 6. Density (top), velocity (middle), and pressure (bottom) profiles for the double rarefaction problem, at $t = 0.1$. Solid line: Finite-volume (FV) scheme. Dashed line: Reference from an exact Riemann solver.

time and the regularized transformation (Sec. IIC) is applied when it is necessary to connect different reference frames. The key point of the current scheme is the computation of the fluxes in the comoving reference frame. This construction, enforced by the predictor-corrector iterative procedure, ensures Galilean invariance and avoids any errors originating from truncated equilibria. While the computational cost is increased relative to the original DUGKS, the operational range of a given lattice is extended greatly without increasing the number of discrete speeds. As shown in the results, extreme compressible flows can be accurately and robustly captured

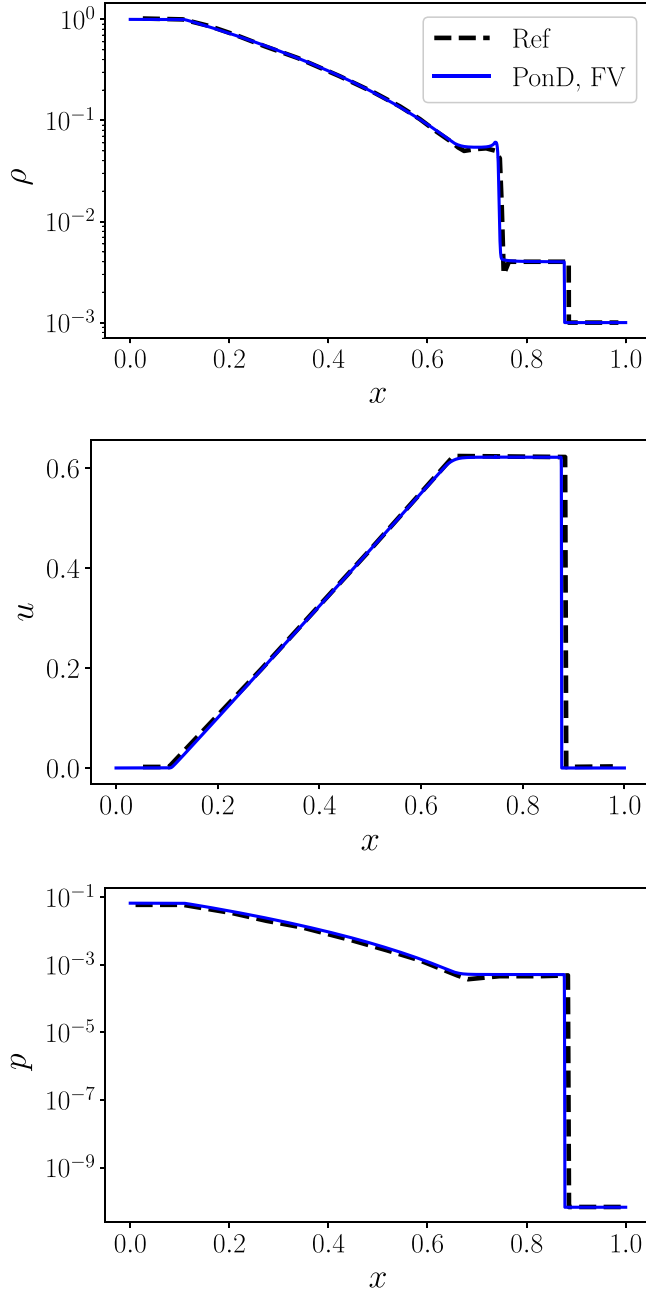


FIG. 7. Density (top), velocity (middle), and pressure (bottom) profiles for the Le Blanc problem, at $t = 6$. Solid line: Finite-volume (FV) scheme. Dashed line: Reference solution [42].

with the $D2Q16$ lattice in a comoving reference frame, which is not feasible if a uniform reference frame is imposed. A comparison of the runtimes between the proposed model and original DUGKS is further discussed in Sec. IV B 6.

IV. RESULTS AND DISCUSSION

In this section we validate our model through one-dimensional (1D) and 2D benchmarks. First we test the model with 1D Riemann problems, involving up to moderate discontinuities. Flows with low density-near vacuum regions and very strong discontinuities are investigated subsequently with

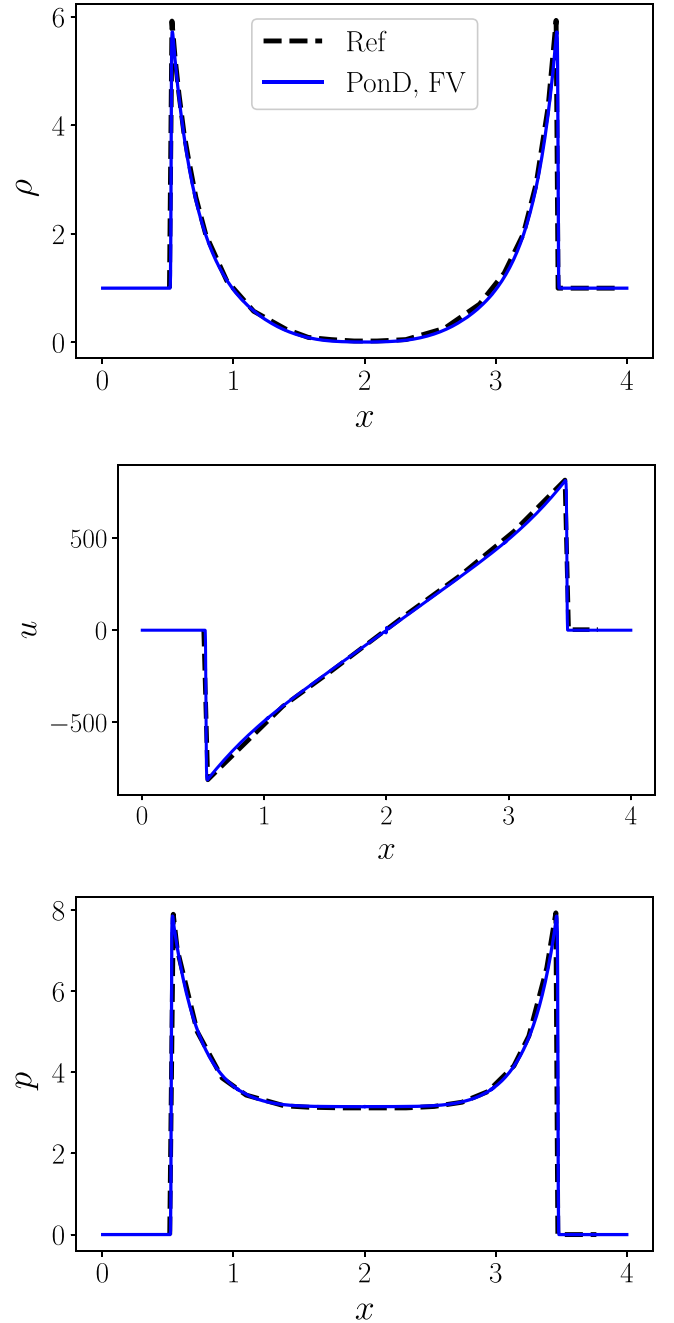


FIG. 8. Density (top), velocity (middle), and pressure (bottom) profiles for the Sedov blast wave problem, at $t = 0.001$. Solid line: Finite-volume (FV) scheme. Dashed line: Reference solution [42].

the finite-volume scheme (Sec. III B). In these flows, where the mass conservation is of high importance, we compare the performance of the two discretization schemes. We conclude the results with classical high Mach 2D problems. Unless stated otherwise, the numerical parameters of the simulations are the following. The time step δt is such that the Courant-Friedrichs-Lewy (CFL) number is $\text{CFL} = \max |v_{i\alpha}|(\delta t/\delta x) = 0.2$, where δx is the grid resolution. The adiabatic exponent is $\gamma = 1.4$. Additionally, the viscosity is low enough such that the results remain invariant [typically $\mu \sim \mathcal{O}(10^{-3}-10^{-2})$]. Finally, we note that the formulation of the initial and bound-

any conditions are based on nondimensional variables, scaled with appropriate reference density, velocity, and pressure.

A. One-dimensional gas dynamic problems with weak to moderate discontinuities

1. Sod's shock tube

In the first case we simulate Sod's shock tube [58], which is a typical benchmark Riemann problem for a compressible flow solver. The initial conditions are

$$(\rho, u, p) = \begin{cases} (1, 0, 0.15), & 0 \leq x < 0.5, \\ (0.125, 0, 0.015), & 0.5 \leq x \leq 1. \end{cases} \quad (53)$$

The resolution of the computational domain is $L = 600$. The results for the density, velocity, and pressure profiles at time $t = 0.2$ are shown in Fig. 1, indicating very good match with the exact solution.

2. Lax problem

We continue with the Lax problem [59], with the following initial conditions:

$$(\rho, u, p) = \begin{cases} (0.445, 0.698, 3.528), & 0 \leq x < 0.5, \\ (0.5, 0, 0.571), & 0.5 \leq x \leq 1. \end{cases} \quad (54)$$

The simulation is performed with $L = 600$, until $t = 0.14$. The results, shown in Fig. 2, compare very well with the exact solution, with the exception of minor oscillations. The presence of numerical oscillations at the contact wave has been also reported at thermal compressible DUGKS simulations, being sensitive to the numerical limiter used for the spatial reconstruction [33].

3. Shock density-wave interaction

In this case, also known as Shu-Osher problem [60], a Mach 3 shock wave interacts with a perturbed density field. The interaction leads to discontinuities and the formation of small structures. The initial conditions are

$$(\rho, u, p) = \begin{cases} (3.857, 2.629, 10.333), & 0 \leq x < 1, \\ (1 + 0.2 \sin(5(x - 5)), 0, 1), & 1 \leq x \leq 10. \end{cases} \quad (55)$$

The results for the density profile, at $t = 1.8$ and $L = 800$, are shown in Fig. 3. It is clear that the shock location and the high-frequency waves are captured very well, apart from a small underestimation of the amplitudes of the postshock waves. The density profile for a simulations with high resolution of $L = 2400$ are also shown in Fig. 3, indicating an excellent match with the reference solution [61].

B. One-dimensional gas dynamic problems with very strong discontinuities

In this section we validate the model against flows with very strong discontinuities. We continue with the finite-volume discretization, the conservative properties of which are important for this regime. A comparison between the semi-Lagrangian and the finite-volume scheme is discussed in the following Sec. IV B 6.

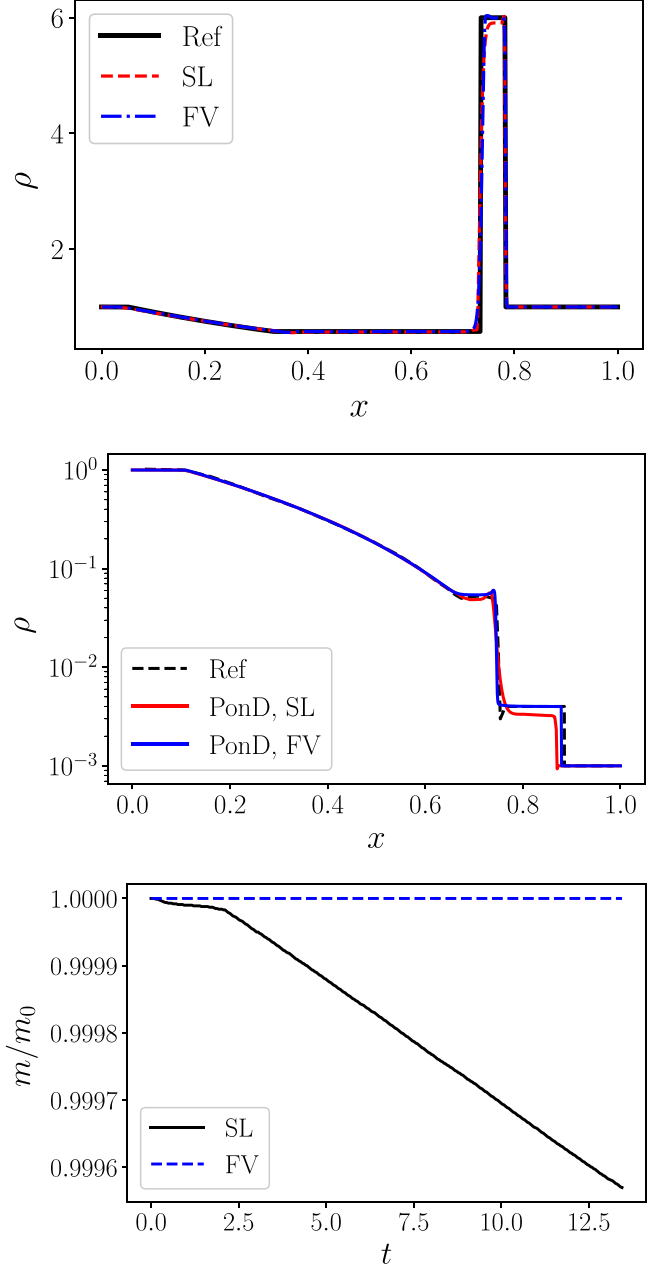


FIG. 9. Comparison of semi-Lagrangian (SL) and finite-volume schemes (FV). Top: Strong shock tube. Middle: Le Blanc problem. Bottom: Evolution of mass for the Le Blanc problem.

1. Strong shock tube

We consider the case of a strong shock tube [62], where the ratio between the temperature of the left and right side is 10^5 . The initial conditions for this problem are

$$(\rho, u, p) = \begin{cases} (1, 0, 1000), & 0 \leq x < 0.5, \\ (1, 0, 0.01), & 0.5 \leq x \leq 1. \end{cases} \quad (56)$$

This problem, characterized by the strong temperature discontinuity and a high Mach number of 198, probes the robustness and accuracy of the numerical methods. The results of the simulation, at $t = 0.012$ and $L = 800$, are shown in

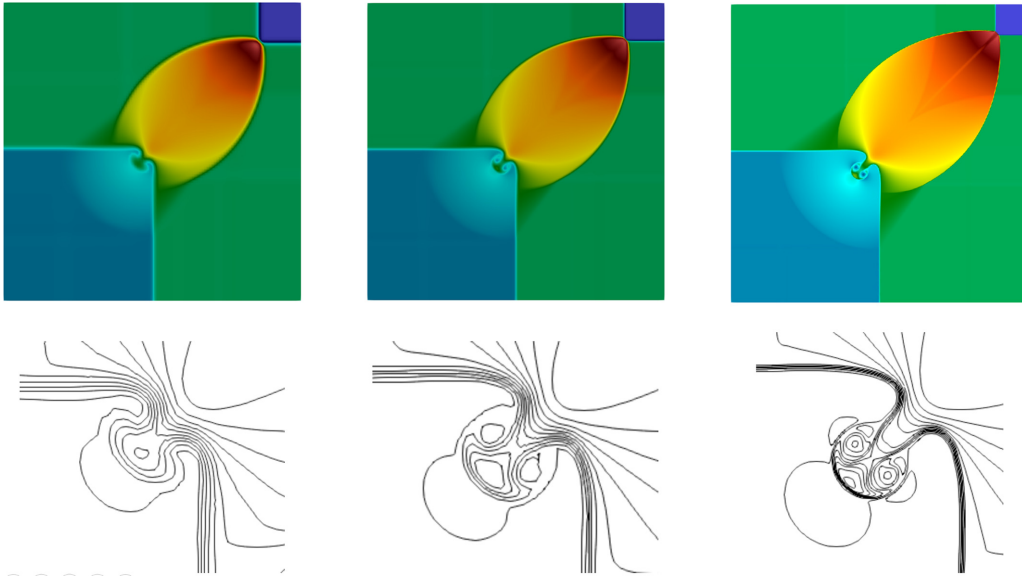


FIG. 10. Two-dimensional Riemann problem with three different resolutions, [125,125] (left), [250,250] (middle), and [750,750] (right). The top row shows plots of the density fields, at $t = 0.25$. The bottom row represent 30 equidistant density contours.

Fig. 4. Overall, a very good agreement with the exact solution is noted.

2. Two blast waves interaction problem

The next test case is the two-blast-wave interaction problem, proposed by Woodward and Colella [63]. The following initial conditions are imposed for this problem:

$$(\rho, u, p) = \begin{cases} (1, 0, 1000), & 0 \leq x < 0.1, \\ (1, 0, 0.01), & 0.1 \leq x < 0.9, \\ (1, 0, 100), & 0.9 \leq x < 1. \end{cases} \quad (57)$$

The resolution is $L = 1600$ and reflective boundary conditions (BCs) are applied at $x = 0$ and $x = 1$. The results at $t = 0.038$, shown in Fig. 5, are in very good agreement with the reference solution from Ref. [42].

3. Double rarefaction problem

We continue with a near-vacuum test case, which is known as the double rarefaction problem [64]. The initial conditions are as follows:

$$(\rho, u, p) = \begin{cases} (1, -2, 0.1), & 0 \leq x < 0.5, \\ (1, 2, 0.1), & 0.5 \leq x \leq 1. \end{cases} \quad (58)$$

The results are compared with the exact solution at $t = 0.1$ and $L = 800$, as shown in Fig. 6. It can be seen that as the two rarefaction waves propagate toward opposite directions, a near-vacuum is formed in the center of the domain. Nonetheless, a good agreement to the reference solution can be observed.

4. Le Blanc problem

The Le Blanc problem is considered next [65], which involves very strong discontinuities and is initialized with the following conditions:

$$(\rho, u, p) = \begin{cases} (1, 0, 2/3 \times 10^{-1}), & 0 \leq x < 3, \\ (10^{-3}, 0, 2/3 \times 10^{-10}), & 3 \leq x \leq 9. \end{cases} \quad (59)$$

In this problem, the adiabatic exponent is fixed to $\gamma = 5/3$. Figure 7 shows the results at $t = 6$ and $L = 4000$. With the exception of minor oscillations, a very good agreement of the present scheme with the reference solution [42] is observed.

5. Planar Sedov blast-wave problem

The final 1D test case is the planar Sedov blast-wave problem [66]. The initial conditions for this case are as follows:

$$(\rho, u, p) = \begin{cases} (1, 0, 2.56 \times 10^8), & 2 - 0.5\delta x \leq x \leq 2 + 0.5\delta x, \\ (10^{-3}, 0, 4 \times 10^{-13}), & \text{otherwise.} \end{cases} \quad (60)$$

The initial conditions of this problem approximate a δ function of pressure, concentrated at the center of the domain and almost vanishing everywhere else. For the implementation, a steep Gaussian distribution of density was imposed, with the same energy input as implied by (60). The blast wave emanating from the center propagates outwards, creating a postshock region of very low density. It is noted that the initial ratio of pressure between the center and the surroundings is 21 orders of magnitude. The results are shown in Fig. 8, at $t = 0.001$ and $L = 1600$, demonstrating very good agreement with the reference solution [42].

6. Comparison of semi-Lagrangian and finite-volume schemes

We compare in this section the two numerical schemes that were used in this work. As mentioned above, the key distinction between the two methods is that the finite-volume discretization is strictly conservative, whereas the semi-Lagrangian method is not. While there exist conservative formulations [52], they have not been the focus of the current work. To highlight the effect through our test cases, we compare the strong shock tube and the Le Blanc problem. The former is characterized by strong discontinuities in pressure and temperature but the density is of the same order. In contrast, the Le Blanc problem involves large variations in the density. Figure 9 compares the results of the two numerical

schemes for these problems. For the case of the strong shock tube, an almost identical profile is attained, with minor oscillations being more pronounced for the semi-Lagrangian scheme. On the other hand, the performance of the two schemes deviates for the case of the Le Blanc problem. Here we notice that the finite-volume discretization leads to a very accurate comparison with the reference solution. However, a discrepancy in density is observed for the semi-Lagrangian scheme. In particular, an under prediction in the density as well as a mismatch of the shock location are present. This behavior is expected for problems involving low densities, since the effect of the conservation error is more pronounced.

We conclude the comparison with a comment regarding the computational efficiency of the two schemes. Comparing the two algorithms, one can notice that per time-step one semi-Lagrangian step is included in the flux calculation for the finite-volume realization. Therefore, the computational cost of the finite-volume scheme, per time step, is in general higher than the semi-Lagrangian scheme. However, the added cost to ensure strict conservation remains reasonable. In particular, we compared the runtimes of the two schemes, for a given level of accuracy (same L_2 error) for the Shu-Osher problem and observed only 20% increase for the finite-volume implementation. We need to stress, however, that a comprehensive study of the computational performance of the two schemes, including efficiency, stability, and numerical dissipation, requires further in-depth investigations and is left for future work.

Finally, we compare the computational efficiency of the finite-volume PonD model with the original DUGKS scheme. The reference frame transformations as well as the predictor-corrector iterations during the flux calculation result in a computational overhead compared with the standard DUGKS scheme. For a quantitative discussion, we measure the runtimes of the schemes, using the Shu-Osher problem. With the same numerical parameters, the runtime of the PonD model is 3.7 times larger than the DUGKS scheme. However, we observe that the PonD model is 2.1 times faster than DUGKS if we compare the two models with the same level of accuracy (same L_2 error).

C. Two-dimensional cases

1. Two-dimensional Riemann problem

As a first validation in two dimensions we simulate a 2D Riemann problem, which is a classical benchmark for compressible flow solvers [67]. A square domain $(x, y) \in [0, 1] \times [0, 1]$ is divided into four quadrants, each of which is initialized with constant values of density, velocity, and pressure as follows:

$$(\rho, u_x, u_y, p) = \begin{cases} (0.5313, 0, 0, 0.4), & x > 0.5, y > 0.5, \\ (1, 0.7276, 0, 1), & x \leq 0.5, y > 0.5, \\ (0.8, 0, 0, 1), & x \leq 0.5, y \leq 0.5, \\ (1, 0, 0.7276, 1), & x > 0.5, y \leq 0.5. \end{cases} \quad (61)$$

At the boundaries, a zero-gradient BC was imposed $\partial_n f = 0$, where \mathbf{n} is the outwards unit normal vector. Three simulations with increasing resolution, $L = 125, 250, 750$, were performed. The results of the density field, as well as den-

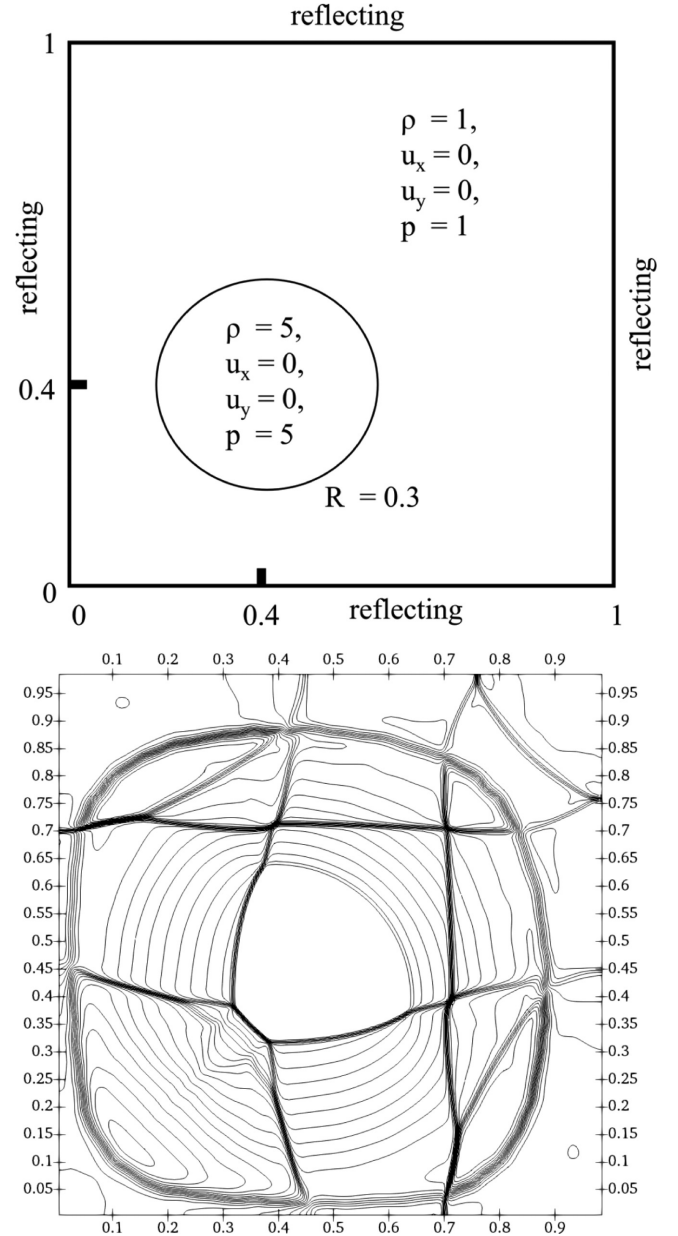


FIG. 11. Top: The configuration of the 2D explosion in a box. Bottom: Thirty equally spaced density contours in the range $\rho \in [0.52, 3.8]$ and at $t = 0.5$ are shown.

sity contours near the center of the domain, are depicted in Fig. 10. The specified initialization of the Riemann problem leads to shock waves interacting and propagating toward the upper right quadrant, while a complex pattern is formed in the opposite direction. The results show a very good agreement with the reference solutions in Refs. [67,68]. Moreover, the refinement of the mesh leads to an increasing resolution of the finer structures near the origin.

2. Two-dimensional explosion in a box

We consider here an unsteady explosion enclosed in a 2D box. The configuration of this case is shown schematically in Fig. 11. The computational domain $[0, 1] \times [0, 1]$ is initial-

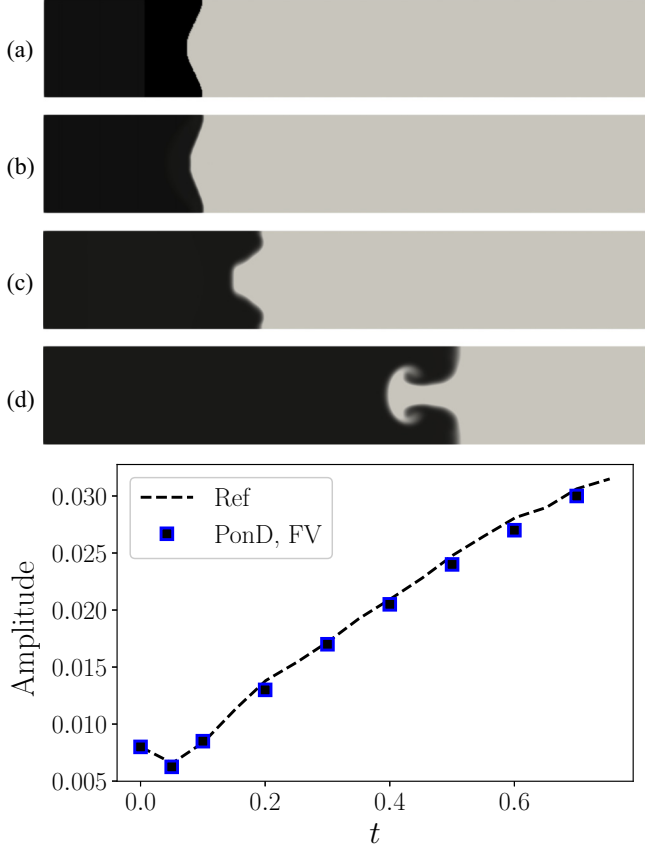


FIG. 12. RMI problem, with the shock wave traveling from the light medium toward the heavy one. Top: Density field at times: $t = 0, 0.06, 0.3, 1.15$. Bottom: Amplitude growth of the instability and comparison with Ref. [71].

ized with the following conditions:

$$(\rho, u_x, u_y, p) = \begin{cases} (5, 0, 0, 5), & |(x, y) - (0.4, 0.4)| < 0.3, \\ (1, 0, 0, 1), & \text{otherwise.} \end{cases} \quad (62)$$

The domain was discretized with 256 points per direction and reflective BCs were imposed on the walls of the box. With this setup, the circular shock waves expand toward the boundaries of the box and the reflected waves interact in a complicated manner. A snapshot from the evolution at $t = 0.5$ is shown in Fig. 11, which depicts 30 density contours. A comparison with the results obtained from a block-structured adaptive mesh refinement solver in Ref. [69] demonstrates an excellent agreement between the observed patterns in the density field.

3. Richtmyer-Meshkov instability

We proceed further with the validation of our model and consider the simulation of the Richtmyer-Meshkov instability (RMI) [70]. In the RMI problem, a shock wave collides with the interface of two fluids with different densities. In the following, we will compare our results with a numerical study of the RMI from Ref. [71].

The first type of RMI problem to consider is the case of a shock wave, with Mach number of 1.2, traveling from the light medium to the heavy one. The computational

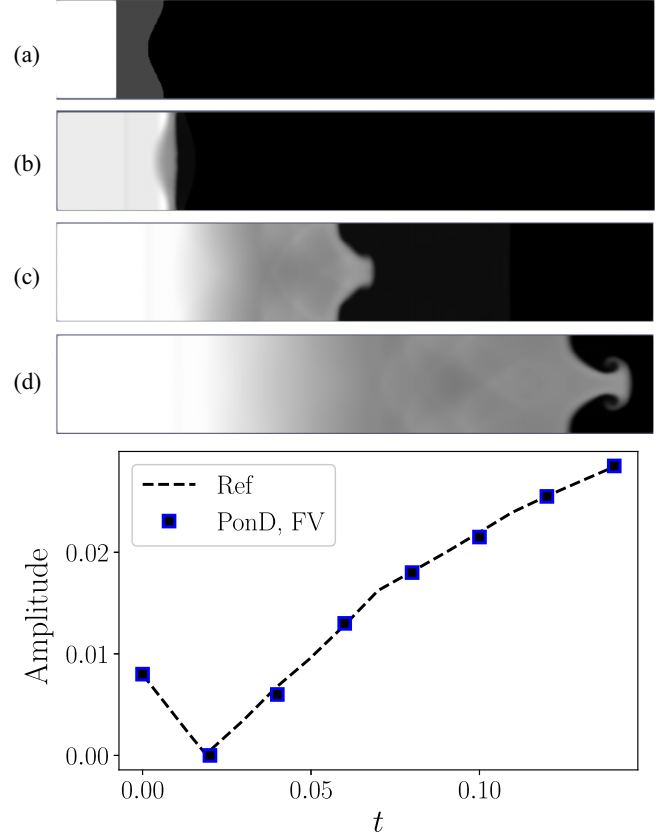


FIG. 13. RMI problem, with the shock wave traveling from the heavy medium toward the light one. Top: Density field at times: $t = 0, 0.02, 0.08, 0.16$. Bottom: Amplitude growth of the instability and comparison with Ref. [71].

domain $[0, 0.6] \times [0, 0.1]$ is initialized with the following conditions:

$$(\rho, u_x, u_y, p) = \begin{cases} (1.34161, 0.361538, 0, 0.151332), & 0 \leq x < 1/6, \\ (1, 0, 0, 1), & 1/6 \leq x < 1/4, \\ (5.04, 0, 0, 1), & \text{otherwise.} \end{cases} \quad (63)$$

Additionally, a sinusoidal perturbation with amplitude of 0.008 is imposed on the interface. The simulation was performed with a grid [600,100]. The numerical setup is concluded with inflow BC on the left boundary, outflow BC on the right boundary and zero-gradient BC at the bottom and top boundaries. The temporal evolution of the instability is captured in Fig. 12, which shows the density field at different times. The simulation compares very well with the corresponding results from Ref. [71]. A quantitative comparison is demonstrated in Fig. 12, which shows the change of the perturbation amplitude with time.

In the second type of the RMI problem, a shock wave with 2.5 Mach number, travels from the heavy medium to the light one. This configuration is achieved with the following initial

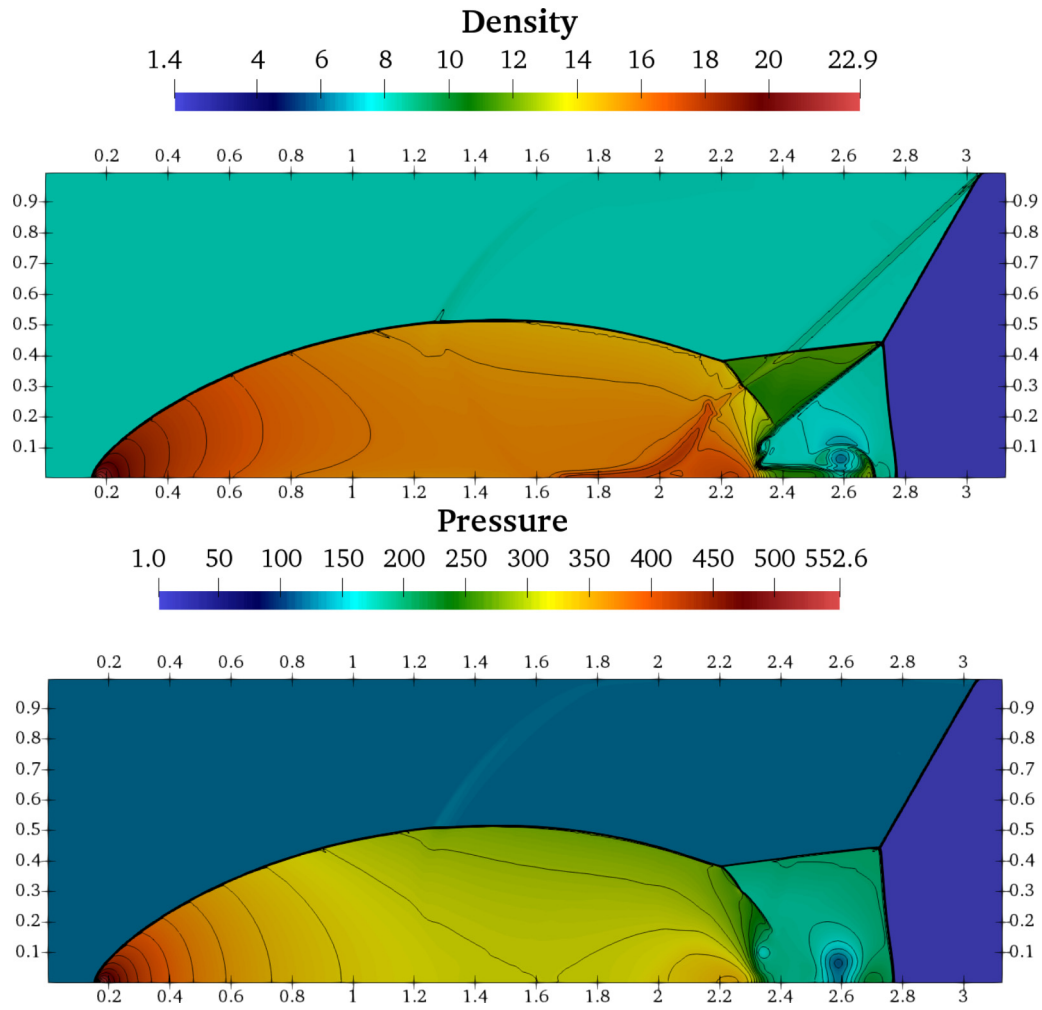


FIG. 14. The double Mach reflection problem. Top: Density field. Bottom: Pressure field.

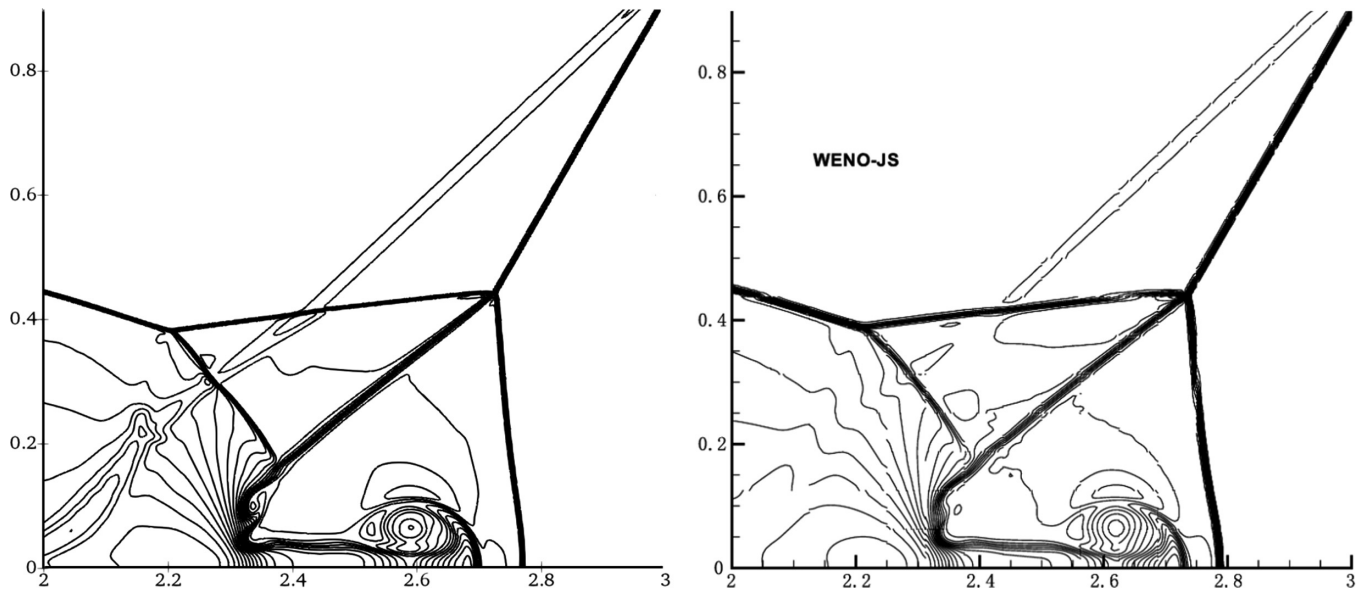


FIG. 15. The double Mach reflection problem. Comparison of 43 density contours of current results (left) with reference [75] (right). Reference figure reprinted from Ref. [75] with permission from Elsevier.

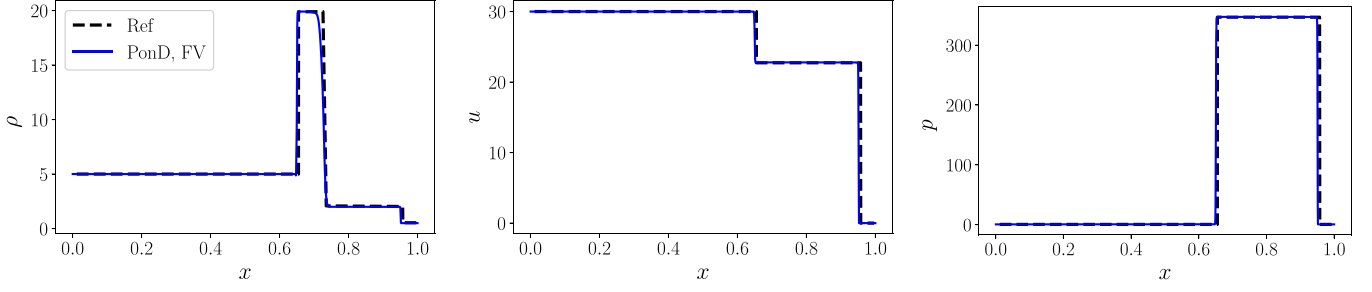


FIG. 16. Density (left), velocity (middle), and pressure (right) profiles for the 1D Riemann “jet,” at $t = 0.06$. Solid line: Finite-volume (FV) scheme. Dashed line: Reference from exact Riemann solver.

conditions:

$$(\rho, u_x, u_y, p) = \begin{cases} (3.33, 2.07, 0, 7.125), & 0 \leq x < 1/12, \\ (1, 0, 0, 1), & 1/12 \leq x < 1/6, \\ (0.138, 0, 0, 1), & \text{otherwise.} \end{cases} \quad (64)$$

Apart from the initial conditions, the numerical setup is the same as in the previous RMI simulation. The results, shown in Fig. 13, are in very good agreement with Ref. [71].

4. Double Mach reflection

The double Mach reflection problem is an important benchmark for compressible solvers, which has been studied extensively experimentally, theoretically and numerically [63,72,73]. In this setup, a Mach 10 shock wave collides with a reflecting wall, which is inclined 30° counterclockwise with respect to the shock propagation direction. The computational domain is a $[0, 4] \times [0, 1]$ rectangle discretized with a resolution [1000,250].

Following the conventional configuration [74], the simulation is initialized with a shock inclined 60° to the horizontal, intersecting the bottom boundary at $x = 1/6$. The undisturbed state of the gas is $(\rho, u_x, u_y, p) = (1.4, 0, 0, 1)$ and the post-shock state $(\rho, u_x, u_y, p) = (8, 4.125\sqrt{3}, -4.125, 116.5)$. At the bottom boundary, the fixed postshock conditions are imposed along $x \in [0, 1/6]$ and reflecting BCs along $x \in [1/6, 4]$. At the left boundary, the fixed postshock conditions are also imposed and on the right boundary zero gradient BCs. At the top boundary, time-dependent BC are specified, which track the motion of the initial Mach 10 shock wave [63].

The results for the density and pressure fields at $t = 0.2$ are shown in Fig. 14, with the flow characteristics being in very good agreement with corresponding results from the literature. Following the impact of the shock wave on the reflecting wall, a self-similar structure is formed and growing along the propagation of the shock. The key features of the flow are distinguished in the results, including the two Mach stems, two triple points, a prime slip line, and a fainter secondary slip line as well as the jet formation near the wall. A comparison of the density and pressure fields with references from the literature [63,74,75], shown in Fig. 15, demonstrate very good match in terms of the feature locations and the magnitude of the hydrodynamic fields.

5. Astrophysical jet

As a final test case, we consider an astrophysical jet of Mach 80, without radiative cooling [43]. This case is an example of actual gas flows revealed from images of the Hubble Space Telescope and therefore is of high scientific interest. Following Ref. [76], we first present a 1D “jet” Riemann problem in a domain $[0, 2, 0]$, with the following initial conditions:

$$(\rho, u, p) = \begin{cases} (5, 30, 0.4127), & 0 \leq x < 0.1, \\ (0.5, 0, 0.4127), & 0.1 \leq x < 2. \end{cases} \quad (65)$$

The results of the simulation with a resolution of 1500 points and $\gamma = 5/3$ are shown in Fig. 16. We continue with the 2D case, according to the configuration in Ref. [43]. The computational domain $[0, 2] \times [-0.5, 0.5]$ is initialized with the following conditions,

$$(\rho, u_x, u_y, p) = \begin{cases} (5, 30, 0, 0.4127), & \text{if } x = 0, -0.05 \leq y \leq 0.05, \\ (0.5, 0, 0, 0.4127), & \text{otherwise.} \end{cases} \quad (66)$$

Outflow BCs are used around the domain, except the left boundary, where the prescribed fixed conditions are imposed. The simulation was performed with resolution [1000,500]. The density, pressure, temperature, and Mach number are shown in Fig. 17, where the bow shock propagating into the surrounding medium is captured.

V. CONCLUSION

In this work, we have presented a PonD model with a revised reference frame transformation using Grad’s projection to enhance stability and accuracy. The resulting scheme was discretized using both a semi-Lagrangian approach as well as a finite-volume realization. For validation, we have selected a number of challenging 1D and 2D test cases to probe accuracy and robustness for flows including very strong pressure and temperature discontinuities, large Mach numbers, and near-vacuum regions. The results show that the proposed kinetic scheme, which is tightly connected to the classical LBM, can indeed capture the highly complex and nonlinear dynamics of high-speed compressible flows with strong discontinuities.

With these encouraging results, a number of possible directions for future work arise. For instance, using an adaptively

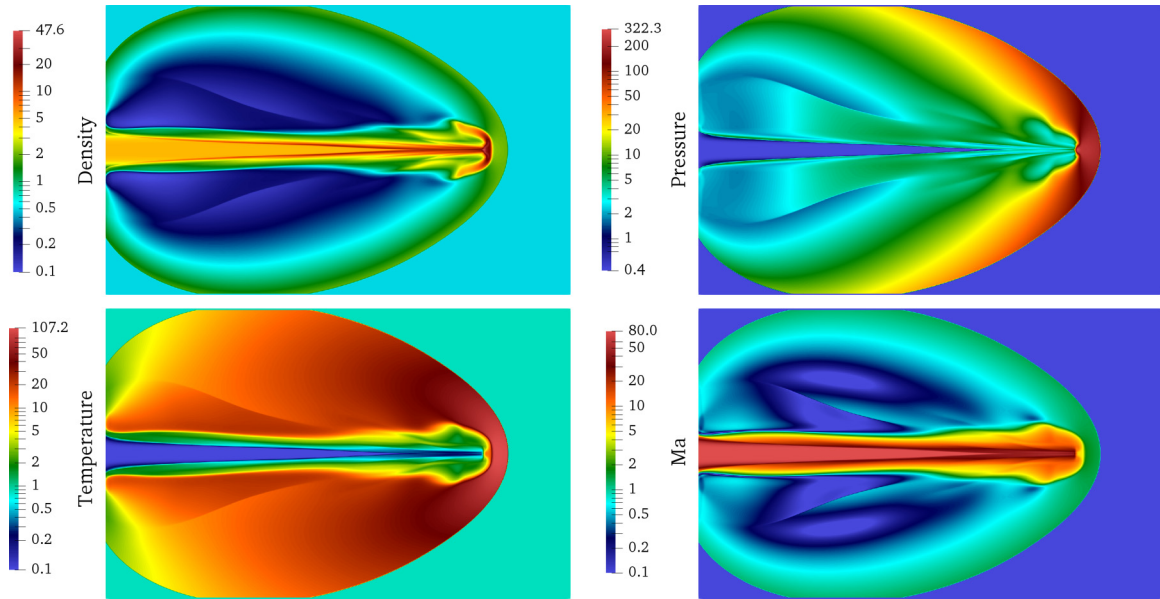


FIG. 17. Astrophysical jet problem. The following fields are plotted: Density (top left), pressure (top right), temperature (bottom left), and Mach number (bottom right).

refined velocity space, in the spirit of Ref. [45], will not only increase efficiency but also extend the scheme to nonequilibrium flows. Furthermore, performance in three dimensions and for flows involving complex geometries shall be assessed in future work.

ACKNOWLEDGMENTS

This work was supported by European Research Council (ERC) Advanced Grant No. 834763-PonD. Computational resources at the Swiss National Super Computing Center CSCS were provided under the Grant No. s1066.

- [1] F. J. Higuera, S. Succi, and R. Benzi, Lattice gas dynamics with enhanced collisions, *Europhys. Lett.* **9**, 345 (1989).
- [2] F. J. Higuera and J. Jiménez, Boltzmann approach to lattice gas simulations, *Europhys. Lett.* **9**, 663 (1989).
- [3] B. Dorschner, S. S. Chikatamarla, and I. V. Karlin, Transitional flows with the entropic lattice Boltzmann method, *J. Fluid Mech.* **824**, 388 (2017).
- [4] B. Dorschner, F. Bösch, S. S. Chikatamarla, K. Boulouchos, and I. V. Karlin, Entropic multi-relaxation time lattice Boltzmann model for complex flows, *J. Fluid Mech.* **801**, 623 (2016).
- [5] X. He, S. Chen, and G. D. Doolen, A novel thermal model for the lattice Boltzmann method in incompressible limit, *J. Comput. Phys.* **146**, 282 (1998).
- [6] Z. Guo, C. Zheng, B. Shi, and T. S. Zhao, Thermal lattice Boltzmann equation for low Mach number flows: Decoupling model, *Phys. Rev. E* **75**, 036704 (2007).
- [7] I. V. Karlin, D. Sichau, and S. S. Chikatamarla, Consistent two-population lattice Boltzmann model for thermal flows, *Phys. Rev. E* **88**, 063310 (2013).
- [8] M. A. Mazloomi, S. S. Chikatamarla, and I. V. Karlin, Entropic Lattice Boltzmann Method for Multiphase Flows, *Phys. Rev. Lett.* **114**, 174502 (2015).
- [9] A. M. Mazloomi, S. S. Chikatamarla, and I. V. Karlin, Drops bouncing off macro-textured superhydrophobic surfaces, *J. Fluid Mech.* **824**, 866 (2017).
- [10] M. Wöhrwag, C. Semperebon, A. Mazloomi Moqaddam, I. Karlin, and H. Kusumaatmaja, Ternary Free-Energy Entropic Lattice Boltzmann Model with a High Density Ratio, *Phys. Rev. Lett.* **120**, 234501 (2018).
- [11] N. Sawant, B. Dorschner, and I. V. Karlin, Consistent lattice Boltzmann model for multicomponent mixtures, *J. Fluid Mech.* **909**, A1 (2021).
- [12] N. Sawant, B. Dorschner, and I. V. Karlin, A lattice Boltzmann model for reactive mixtures, *Philos. Trans. R. Soc. A* **379**, 20200402 (2021).
- [13] X. Shan, X.-F. Yuan, and H. Chen, Kinetic theory representation of hydrodynamics: A way beyond the Navier–Stokes equation, *J. Fluid Mech.* **550**, 413 (2006).
- [14] K. V. Sharma, R. Straka, and F. W. Tavares, Current status of lattice Boltzmann methods applied to aerodynamic, aeroacoustic, and thermal flows, *Prog. Aeronaut. Sci.* **115**, 100616 (2020).
- [15] T. Krueger, H. Kusumaatmaja, A. Kuzmin, O. Shardt, G. Silva, and E. Viggen, *The Lattice Boltzmann Method: Principles and Practice*, Graduate Texts in Physics (Springer, Berlin, 2016).
- [16] S. Succi, *The Lattice Boltzmann Equation: For Complex States of Flowing Matter* (Oxford University Press, Oxford, 2018).
- [17] S. S. Chikatamarla and I. V. Karlin, Entropy and Galilean Invariance of Lattice Boltzmann Theories, *Phys. Rev. Lett.* **97**, 190601 (2006).
- [18] S. S. Chikatamarla and I. V. Karlin, Lattices for the lattice Boltzmann method, *Phys. Rev. E* **79**, 046701 (2009).

- [19] F. J. Alexander, S. Chen, and J. D. Sterling, Lattice Boltzmann thermohydrodynamics, *Phys. Rev. E* **47**, R2249(R) (1993).
- [20] N. Frapolli, S. S. Chikatamarla, and I. V. Karlin, Entropic lattice Boltzmann model for compressible flows, *Phys. Rev. E* **92**, 061301(R) (2015).
- [21] N. Frapolli, S. S. Chikatamarla, and I. V. Karlin, Entropic lattice Boltzmann model for gas dynamics: Theory, boundary conditions, and implementation, *Phys. Rev. E* **93**, 063302 (2016).
- [22] N. I. Prasianakis and I. V. Karlin, Lattice Boltzmann method for thermal flow simulation on standard lattices, *Phys. Rev. E* **76**, 016702 (2007).
- [23] M. H. Saadat, F. Bösch, and I. V. Karlin, Lattice Boltzmann model for compressible flows on standard lattices: Variable Prandtl number and adiabatic exponent, *Phys. Rev. E* **99**, 013306 (2019).
- [24] M. H. Saadat, B. Dorschner, and I. Karlin, Extended lattice Boltzmann model, *Entropy* **23**, 475 (2021).
- [25] M. H. Saadat, S. A. Hosseini, B. Dorschner, and I. V. Karlin, Extended lattice Boltzmann model for gas dynamics, *Phys. Fluids* **33**, 046104 (2021).
- [26] A. Bardow, I. V. Karlin, and A. A. Gusev, General characteristic-based algorithm for off-lattice Boltzmann simulations, *Europhys. Lett.* **75**, 434 (2006).
- [27] C. Shu, X. D. Niu, and Y. T. Chew, Taylor-series expansion and least-squares-based lattice Boltzmann method: Two-dimensional formulation and its applications, *Phys. Rev. E* **65**, 036708 (2002).
- [28] M. Cheng and K. C. Hung, Lattice Boltzmann method on nonuniform mesh, *Int. J. Comput. Methods Eng. Sci. Mech.* **05**, 291 (2004).
- [29] A. Krämer, K. Küllmer, D. Reith, W. Joppich, and H. Foysi, Semi-Lagrangian off-lattice Boltzmann method for weakly compressible flows, *Phys. Rev. E* **95**, 023305 (2017).
- [30] D. Wilde, A. Krämer, D. Reith, and H. Foysi, Semi-Lagrangian lattice Boltzmann method for compressible flows, *Phys. Rev. E* **101**, 053306 (2020).
- [31] D. Wilde, A. Krämer, D. Reith, and H. Foysi, High-order semi-Lagrangian kinetic scheme for compressible turbulence, *Phys. Rev. E* **104**, 025301 (2021).
- [32] Z. Guo, K. Xu, and R. Wang, Discrete unified gas kinetic scheme for all Knudsen number flows: Low-speed isothermal case, *Phys. Rev. E* **88**, 033305 (2013).
- [33] Z. Guo, R. Wang, and K. Xu, Discrete unified gas kinetic scheme for all Knudsen number flows. ii. thermal compressible case, *Phys. Rev. E* **91**, 033313 (2015).
- [34] Y. Gan, A. Xu, G. Zhang, Y. Zhang, and S. Succi, Discrete Boltzmann trans-scale modeling of high-speed compressible flows, *Phys. Rev. E* **97**, 053312 (2018).
- [35] Y. Ji, C. Lin, and K. H. Luo, Three-dimensional multiple-relaxation-time discrete Boltzmann model of compressible reactive flows with nonequilibrium effects, *AIP Adv.* **11**, 045217 (2021).
- [36] Y. Gan, A. Xu, G. Zhang, and S. Succi, Discrete Boltzmann modeling of multiphase flows: Hydrodynamic and thermodynamic non-equilibrium effects, *Soft Matter* **11**, 5336 (2015).
- [37] H. Lai, A. Xu, G. Zhang, Y. Gan, Y. Ying, and S. Succi, Nonequilibrium thermohydrodynamic effects on the Rayleigh-Taylor instability in compressible flows, *Phys. Rev. E* **94**, 023106 (2016).
- [38] M. La Rocca, A. Montessori, P. Prestininzi, and S. Succi, A multispeed discrete Boltzmann model for transcritical 2d shallow water flows, *J. Comput. Phys.* **284**, 117 (2015).
- [39] N. Frapolli, S. S. Chikatamarla, and I. V. Karlin, Lattice Kinetic Theory in a Comoving Galilean Reference Frame, *Phys. Rev. Lett.* **117**, 010604 (2016).
- [40] B. Dorschner, F. Bösch, and I. V. Karlin, Particles on Demand for Kinetic Theory, *Phys. Rev. Lett.* **121**, 130602 (2018).
- [41] E. Zipunova, A. Perepelkina, A. Zakirov, and S. Khilkov, Regularization and the particles-on-demand method for the solution of the discrete Boltzmann equation, *J. Comput. Sci.* **53**, 101376 (2021).
- [42] L. Fu, A very-high-order TENO scheme for all-speed gas dynamics and turbulence, *Comput. Phys. Commun.* **244**, 117 (2019).
- [43] X. Zhang and C.-W. Shu, On positivity-preserving high order discontinuous Galerkin schemes for compressible Euler equations on rectangular meshes, *J. Comput. Phys.* **229**, 8918 (2010).
- [44] X. Zhang and C.-W. Shu, Positivity-preserving high order finite difference WENO schemes for compressible Euler equations, *J. Comput. Phys.* **231**, 2245 (2012).
- [45] N. G. Kallikounis, B. Dorschner, and I. V. Karlin, Multiscale semi-Lagrangian lattice Boltzmann method, *Phys. Rev. E* **103**, 063305 (2021).
- [46] E. Zipunova, A. Perepelkina, and A. Zakirov, Applicability of regularized particles-on-demand method to solve Riemann problem, *J. Phys.: Conf. Ser.* **1740**, 012024 (2021).
- [47] A. N. Gorbunov and I. V. Karlin, *Invariant Manifolds for Physical and Chemical Kinetics* (Springer-Verlag, Berlin, 2005).
- [48] E. Reyhanian, B. Dorschner, and I. V. Karlin, Thermokinetic lattice Boltzmann model of nonideal fluids, *Phys. Rev. E* **102**, 020103(R) (2020).
- [49] E. Reyhanian, B. Dorschner, and I. Karlin, Kinetic simulations of compressible non-ideal fluids: From supercritical flows to phase-change and exotic behavior, *Computation* **9**, 13 (2021).
- [50] X. He, X. Shan, and G. D. Doolen, Discrete Boltzmann equation model for nonideal gases, *Phys. Rev. E* **57**, R13(R) (1998).
- [51] E. Reyhanian, Thermokinetic model for compressible generic fluids, Ph.D. thesis, ETH Zürich, 2021.
- [52] M. Lentine, J. T. Grétarsson, and R. Fedkiw, An unconditionally stable fully conservative semi-Lagrangian method, *J. Comput. Phys.* **230**, 2857 (2011).
- [53] F. Xiao and T. Yabe, Completely conservative and oscillationless semi-Lagrangian schemes for advection transportation, *J. Comput. Phys.* **170**, 498 (2001).
- [54] Z. Guo and K. Xu, Progress of discrete unified gas-kinetic scheme for multiscale flows, *Adv. Aerodynam.* **3**, 6 (2021).
- [55] B. Van Leer, Towards the ultimate conservative difference scheme. iv. A new approach to numerical convection, *J. Comput. Phys.* **23**, 276 (1977).
- [56] P. L. Roe, Characteristic-based schemes for the Euler equations, *Annu. Rev. Fluid Mech.* **18**, 337 (1986).
- [57] B. van Leer, Towards the ultimate conservative difference scheme. V. A second-order sequel to Godunov's method, *J. Comput. Phys.* **32**, 101 (1979).
- [58] G. A. Sod, A survey of several finite difference methods for systems of nonlinear hyperbolic conservation laws, *J. Comput. Phys.* **27**, 1 (1978).

- [59] P. D. Lax, Weak solutions of nonlinear hyperbolic equations and their numerical computation, *Commun. Pure Appl. Math.* **7**, 159 (1954).
- [60] C.-W. Shu and S. Osher, Efficient implementation of essentially non-oscillatory shock-capturing schemes, ii, *J. Comput. Phys.* **83**, 32 (1989).
- [61] Finite-difference hyperbolic-parabolic PDE solver on cartesian grids, <http://hypar.github.io/>.
- [62] E. Toro and M. Vázquez-Cendón, Flux splitting schemes for the Euler equations, *Comput. Fluids* **70**, 1 (2012).
- [63] P. Woodward and P. Colella, The numerical simulation of two-dimensional fluid flow with strong shocks, *J. Comput. Phys.* **54**, 115 (1984).
- [64] X. Y. Hu, N. A. Adams, and C.-W. Shu, Positivity-preserving method for high-order conservative schemes solving compressible Euler equations, *J. Comput. Phys.* **242**, 169 (2013).
- [65] R. Loubère and M. J. Shashkov, A subcell remapping method on staggered polygonal grids for arbitrary-Lagrangian-Eulerian methods, *J. Comput. Phys.* **209**, 105 (2005).
- [66] L. I. Sedov, *Similarity and Dimensional Methods in Mechanics* (CRC Press, Boca Raton, FL, 1993).
- [67] P. D. Lax and X.-D. Liu, Solution of two-dimensional Riemann problems of gas dynamics by positive schemes, *SIAM J. Sci. Comput.* **19**, 319 (1998).
- [68] A. Kurganov and E. Tadmor, Solution of two-dimensional Riemann problems for gas dynamics without Riemann problem solvers, *Numer. Methods Partial Differ. Equat.* **18**, 584 (2002).
- [69] Amroc-blockstructured adaptive mesh refinement in object-oriented c++, http://amroc.sourceforge.net/examples/euler/2d/html/box_n.htm.
- [70] M. Brouillette, The Richtmyer-Meshkov instability, *Annu. Rev. Fluid Mech.* **34**, 445 (2002).
- [71] F. Chen, A.-G. Xu, G.-C. Zhang, and Y.-J. Li, Multiple-relaxation-time lattice Boltzmann approach to Richtmyer—Meshkov instability, *Commun. Theor. Phys.* **55**, 325 (2011).
- [72] G. Ben-Dor and I. I. Glass, Domains and boundaries of non-stationary oblique shock-wave reflexions. 1. Diatomic gas, *J. Fluid Mech.* **92**, 459 (1979).
- [73] G. Ben-Dor, *Shock Wave Reflection Phenomena* (Springer-Verlag, Berlin, 2007).
- [74] U. S. Vevek, B. Zang, and T. H. New, On alternative setups of the double Mach reflection problem, *J. Sci. Comput.* **78**, 1291 (2019).
- [75] L. Fu, X. Y. Hu, and N. A. Adams, A family of high-order targeted ENO schemes for compressible-fluid simulations, *J. Comput. Phys.* **305**, 333 (2016).
- [76] Y. Ha and C. L. Gardner, Positive scheme numerical simulation of high Mach number astrophysical jets, *J. Sci. Comput.* **34**, 247 (2008).